Zeitschrift: Eclogae Geologicae Helvetiae
Herausgeber: Schweizerische Geologische Gesellschaft
Band: 83 (1990)
Heft: 3: The Hans Laubscher volume

Artikel: Geometry and kinematics of fault-propagation folding
Autor: Suppe, John / Medwedeff, Donald A.
DOI: https://doi.org/10.5169/seals-166595

Eclogae geol. Helv. 83/3: 409–454 (1990)

0012-9402/90/030409–46 $ 1.50 + 0.20/0
Birkhäuser Verlag, Basel

Geometry and kinematics of fault-propagation folding[1])

By John Suppe and Donald A. Medwedeff[2])

Key words: fault-propagation folding, fault-related folding, thrust faulting, fold-and-thrust belts, cross sections, balancing, kinematics, growth structure, Papua New Guinea, Taiwan, Ventura basin.

ABSTRACT

It is here proposed that some thrust faults do not propagate rapidly as clean fractures but rather propagate gradually as slip accumulates. At each instant during propagation, slip goes to zero at the fault tip and is consumed in folding. This kinematic process is here called *fault-propagation folding* and is put forward as an explanation for the common association of asymmetric folds with one steep or overturned limb adjacent to thrust faults.

Two quantitative geometric and kinematic models of fault-propagation folding are derived which encompass the principal expected properties of fault-propagation folding under brittle conditions, one based on conservation of layer thickness and bed length, and the other allowing thickening or thinning of beds in the steep front fold limb. These two models predict qualitatively several observed properties of natural fault-propagation folds. Furthermore the models are in good quantitative agreement with observed shapes of a number of reasonably well documented structures. In many, but not all cases the constant-thickness theory agrees best with the data.

Both models of fault-propagation folding have the kinematic property of self-similar growth by kink-band migration; that is, the fold always has the same shape and position relative to the propagating fault tip but grows in size by beds rolling through kink-band boundaries. These kinematic predictions are tested by consideration of the shapes of fault-propagation folds that grow during sedimentation. The kink bands are predicted to narrow upward within strata deposited during growth. Seismic profiles of several growth fault-propagation folds are in qualitative agreement with the predicted growth structure.

Many fault-propagation folds cease to propagate self-similarly, at which point the fault breaks through the structure, typically along a decollement or within the steep limb, leaving fragments of steep to overturned synclines in the footwall and steep to overturned anticlines in the hanging wall. Such fragments of tight, asymmetric folds adjacent to thrust faults have in the past been considered by some to be drag folds, whereas here we suggest that they are characteristic of the folding mechanism of fault propagation.

The general qualitative and quantitative agreement between the predicted and observed shapes of folds in both preexisting and growth strata provides strong support for the hypothesis of fault-propagation folding.

---

[1]) The contents of this paper will be included in modified form in a book on fault-related folding by John Suppe;

[2]) Department of Geological and Geophysical Sciences, Guyot Hall, Princeton University, Princeton, New Jersey 08544, USA. Present address for Medwedeff: ARCO Oil and Gas Company, 2300 West Plano Parkway, Plano, Texas 75075, USA.

ZUSAMMENFASSUNG

Es wird postuliert, dass sich gewisse Überschiebungsflächen nicht sofort als saubere durchgehende Brüche entwickeln, sondern vielmehr als Ansammlung einzelner Gleitflächen langsam wachsen. In jedem Stadium der Bruchbildung reduziert sich der Versetzungsbetrag in Richtung Überschiebungsfront auf Null, und die Versetzung wird zunehmend durch Faltung kompensiert. Dieser kinematische Prozess wird hier als *fault-propagation folding*, d.h. als Faltung induziert durch Überschiebungswachstum, bezeichnet und wird als Erklärung für asymmetrische Falten mit einem steilen, bzw. überkippten, an eine Überschiebung angrenzenden Schenkel vorgeschlagen.

Zwei quantitative geometrische und kinematische Modelle für *fault-propagation folding*, die die wichtigsten Eigenschaften solcher Falten beschreiben, werden hergeleitet. Beide Modelle gelten für den spröden Deformationsbereich, wobei das eine auf der Erhaltung der Schichtmächtigkeiten und -längen basiert, während das andere mögliche Schichtverdickungen und -verdünnungen im steilen frontalen Schenkel mit in Betracht zieht. Beide Modelle postulieren qualitativ viele tatsächlich beobachtete Phänomene natürlicher *fault-propagation folds*. Zudem stimmen sie mit den beobachteten Geometrien einer nicht unbedeutenden Zahl gut dokumentierter Strukturen auch quantitativ überein, wobei in den meisten Fällen das erste, auf konstanter Schichtmächtigkeit basierende Modell die bessere Übereinstimmung mit den beobachteten Daten zeigt.

Beide Modelle haben die kinematische Eigenschaft, durch Knickband-Migration zu wachsen, wobei die Falte ihre Form und ihre relative Position zur Front der Überschiebung während allen Verformungsschritten beibehält (*self-similar growth*) und durch das Wandern der Schichten durch die Scharniere hindurch wächst. Diese kinematischen Postulate werden anhand der Geometrien von *fault-propagation folds* getestet, die während der Sedimentation wachsen. Die Knickbänder sollten in diesem Fall in den Schichten, die während des Faltenwachstums abgelagert wurden, nach oben hin enger werden. Ein Phänomen, das auf seismischen Profilen etlicher im Wachstum begriffener *fault-propagation folds* auch tatsächlich beobachtet werden kann.

Das Wachstum unter Beibehaltung der Geometrie (*self-similar growth*) vieler *fault-propagation folds* hört an einem bestimmten Punkt auf, und die Überschiebungen durchschlagen die Falte, typischerweise entlang eines Abscherhorizontes oder durch den steilen Faltenschenkel hindurch. Im Liegenden der Überschiebung werden Fragmente von steilen bis überkippten Synklinalen, im Hangenden von steilen bis überkippten Antiklinalen zurückgelassen. Während in der Vergangenheit solche Fragmente oft als Schleppungen interpretiert wurden, sehen wir sie hier als charakteristische Strukturen im Zusammenhang mit wachsenden Überschiebungen an.

Die gute qualitative und quantitative Übereinstimmung zwischen den Voraussagen und den beobachteten Geometrien von natürlichen Falten sowohl in Schichten, die vor, als auch in solchen, die während der Faltung abgelagert wurden, sind wohl die besten Argumente für die geologische Relevanz der *fault-propagation fold*-Hypothese.

Introduction

Asymmetric folds with one steep or overturned limb are common adjacent to thrust faults, for example see Figure 1 from the Brooks Range of Alaska. We propose that such folds form and grow at the tips of the thrust faults as they propagate (*fault-propagation folding* of Suppe 1983a, 1985; Suppe & Medwedeff 1984), but other explanations are reviewed briefly below.

Explanations of the association of thrust faults and asymmetric folds may be summarized as: (1) the folds form first, (2) the faults first, or (3) contemporaneous folding and faulting.

1.1 Folding before fault propagation

The fold forms first by buckling and is later cut by a thrust according to the *breakthrust* model (for example Willis & Willis 1934); there is apparently no direct relationship between the shape of the fold and the shape of the fault (Fig. 2). The idea of a *stretch thrust* is similar (Fig. 3); the overturned limb of a ductile asymmetric fold stretches until it breaks into a thrust (Heim 1919). More recent applications of the fold-first concept include Harris (1970) and Wiltschko & Eastman (1983).

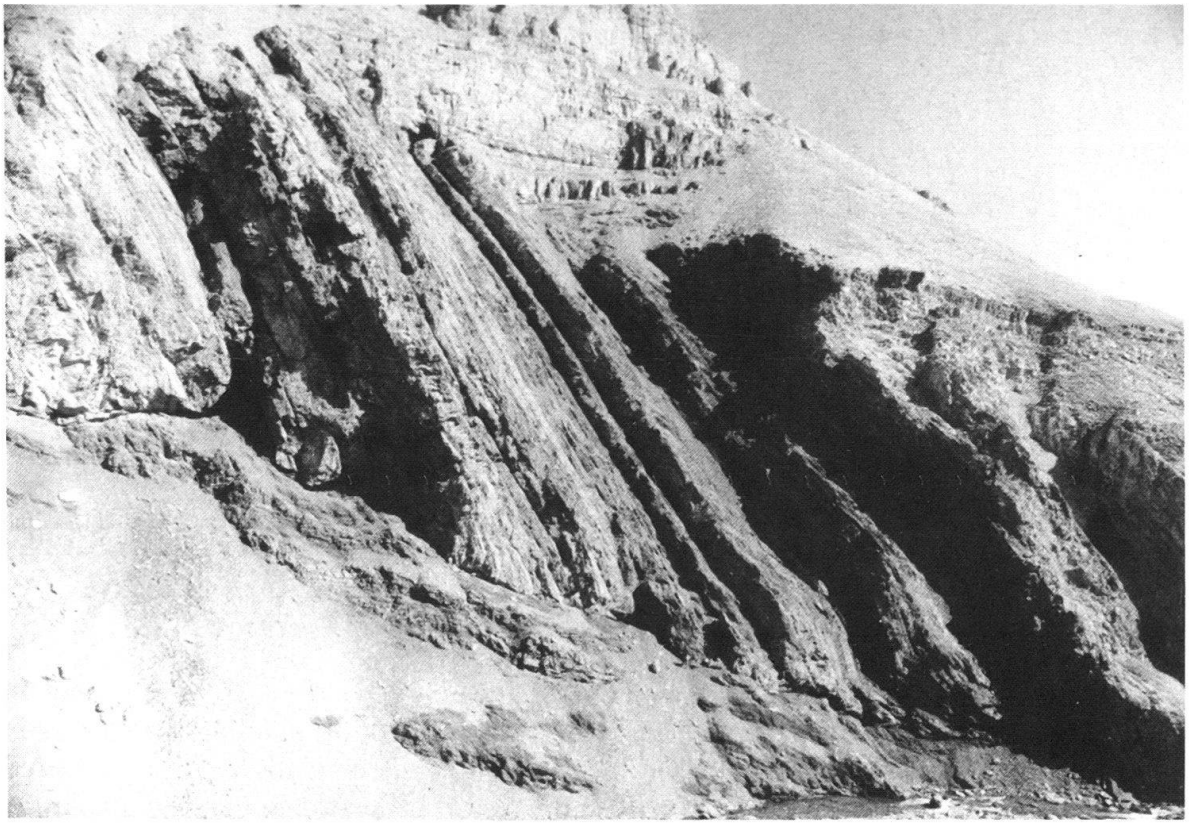

Fig. 1. Angular asymmetric anticline of Mississippian Lisburne Limestone in the hanging wall of a thrust fault, Akmagolik Creek, near Anaktuvuk Pass central Brooks Range, Alaska. The thrust is approximately parallel to bedding in the footwall in shale of the Triassic Siksikpuk Formation. The structure of this outcrop has been described by Ave'Lallement et al. (1987).

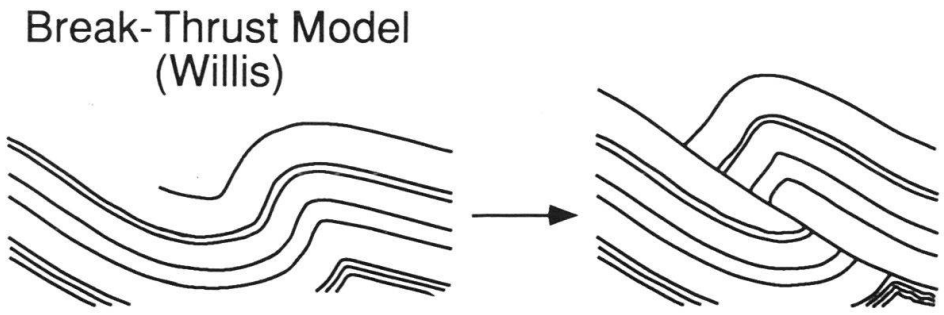

Fig. 2. Break-thrust model for the development of asymmetric anticlines with faulted forelimbs (after Willis & Willis 1934).

1.2 Fault propagation before folding

Some proponents of faulting first have interpreted the asymmetric anticlines in the hanging walls of thrust faults to form by *drag folding* (for example Fox 1959; Benvenuto & Price 1979; Berger & Johnson 1980); a through-going fracture is con-

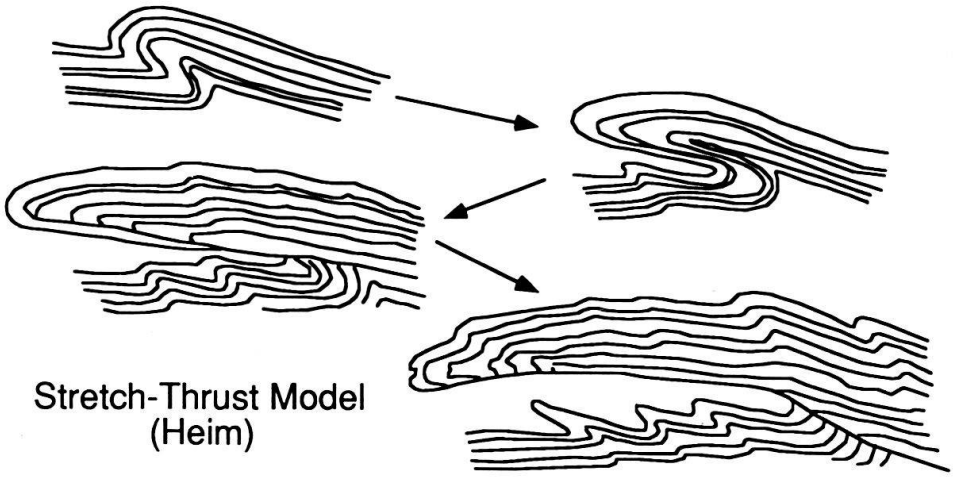

Fig. 3. Stretch-thrust model of development of asymmetric anticlines by faulting of the tectonically thinned forelimb (after HEIM 1919).

sidered to form first, then the less competent formations are progressively bent in response to the frictional resistance of the fault surface, producing a fold that verges in the direction of tectonic transport. No general one-to-one relationship is expected between fold shape and fault shape because the fold evolves progressively with slip. A second model that produces folding in response to slip on a preexisting fault is *fault-bend folding,* in which slip on a non-planar fault produces bends in the hanging-wall block (for example: RICH 1932; DOUGLAS 1955; DAHLSTROM 1970). Fault-bend folding predicts a specific relationship between fault shape and fold shape (SUPPE 1983b); however, the process normally produces shallow dips and does not properly explain hanging-wall anticlines and footwall synclines with steep to overturned limbs such as shown in Figure 1.

1.3 Simultaneous folding and fault propagation

The proponents of contemporaneous folding and faulting consider these steep to overturned folds to form and grow at the tips of propagating thrust faults (Fig. 2); this concept has been called *fault-propagation folding* (SUPPE 1983a, 1985; SUPPE & MEDWEDEFF 1984). A complete kinematic model of fault-propagation folding has not been available until now, but the concept is implicit in the work of several researchers. For example DAHLSTROM (1970) writes in his paper on foothills structure:

> "The original cut-off angles visualized in the stair-step hypothesis must be relatively shallow, to provide a low-friction sliding surface, but the cut-off angles on fore-limb faults are often ninety degrees or even overturned. Such evidence suggests (but does not prove) folding prior to thrusting, because interbed slippage caused by post-thrust folding can increase the cut-off angles drastically. Displacement exchange is a more promising criterion. Field cross-sections at Turner Valley (Fig. 4) show that in this structure the shortening in the deep horizons is accomplished

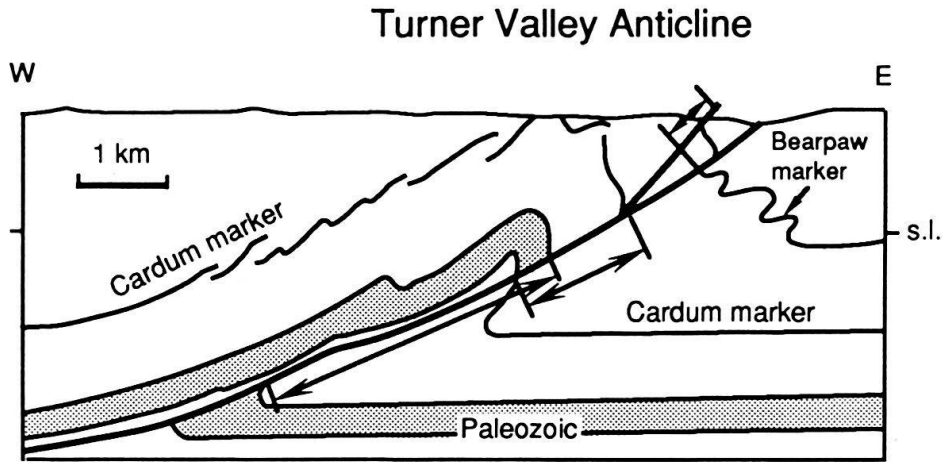

Fig. 4. Cross section of Turner Valley structure, Alberta discussed by DAHLSTROM (1970), as quoted in text.

> primarily by faulting, whereas in the upper horizons a comparable amount of shortening is provided by folding. The balance between diminishing fault throw and increasing vertical-fold limb shows that the fault was propagating itself upward in a growing fold. In such structures, and at a specific marker horizon, the sequence is clearly: fold first, fault second."

The three-dimensional nature of fault propagation and associated fault-tip phenomena were discussed by ELLIOT (1976) who made an analogy between fault tips and crystal dislocations and suggested the presence of a "ductile bead" of folding and/or penetrative strain along the fault tip. BROWN & SPANG (1978) and STOCKMAL (1979) address the relationship of folds to thrust-fault propagation in the description and analysis of fold terminations of thrust faults in the Front Ranges of the Canadian Rockies. WILLIAMS & CHAPMAN (1983) developed a relationship between displacement and distance along a fault, toward the fault tip. The decrease in slip is ascribed to strain in the hanging wall.

Another class of structures that possibly forms by a fault-propagation folding mechanism are the tight to overturned monoclinal flexures in sedimentary cover rocks above faulted basement block uplifts. These structures have been explained by the model of *drape folding* or *forced folding* (for example PRUCHA et al. 1965; STEARNS 1971, 1978; MATTHEWS 1978) in which the cover rocks passively bend to conform to steep faults in the basement. It is now known that at least some of these structures involve low-angle thrusts in the basement (for example BERG 1962; GRIES 1983). These basement-involved structures have a complex origin that is quite unlike the sediment-involved fault-propagation folds that are the focus of this paper and will not be discussed further (for example, NARR & SUPPE 1989; NARR 1990).

It is remarkable that fault-propagation folds have not been widely recognized, yet they appear to be very widespread. This lack of recognition and understanding seems to have three causes: (1) these structures are rarely observed directly in their entirety in cross-sectional views, (2) steep limbs are not normally imaged in seismic sections, and

(3) later faulting commonly breaks through the fold as deformation progresses and obscures the original fault-propagation origin. Fault-propagation folds are normally seen in fragmentary form. Different aspects of fault-propagation folding have been given such names as break thrusts, fold faults, blind thrusts, nappes, and drag folds.

In the following sections we present (1) a qualitative description of the main phenomena of fault-propagation folding using simple geometric models and geologic examples, (2) the derivations of two quantitative geometric and kinematic theories that relate fault shape to fold shape, based on two different conservation assumptions, and (3) a testing of the theories by comparing fold shapes with the predictions of the theories for both preexisting strata and strata deposited during deformation.

2. Qualitative description of fault-propagation folds

2.1 Simple-step fault-propagation folds

Fault-propagation folds are folds that form and grow at the tips of propagating thrust faults (Suppe 1983a, 1985; Suppe & Medwedeff 1984). As a fault continues to propagate, the fold continues to grow at the fault tip. A fold interpreted to form by a fault-propagation mechanism is shown in Figure 5 from the anthracite coal basin of Pennsylvania (Danilchik et al. 1955). The structure is well-known because the coal beds have been mined out. Note that coal beds 6 through 9 have an offset of more than 200 meters along the Suffolk thrust whereas bed 10 shows essentially no offset. Between beds 9 and 10 the slip on the thrust has gone nearly to zero and the slip has been consumed in the anticlinal fold.

A balanced structural model of the progressive development of a fault-propagation fold is shown in Figure 6. The model is quantitatively accurate, retrodeformable, and incorporates many of the essential features of natural fault-propagation folding. It is based on the quantitative theory presented in a later section. In the upper figure the

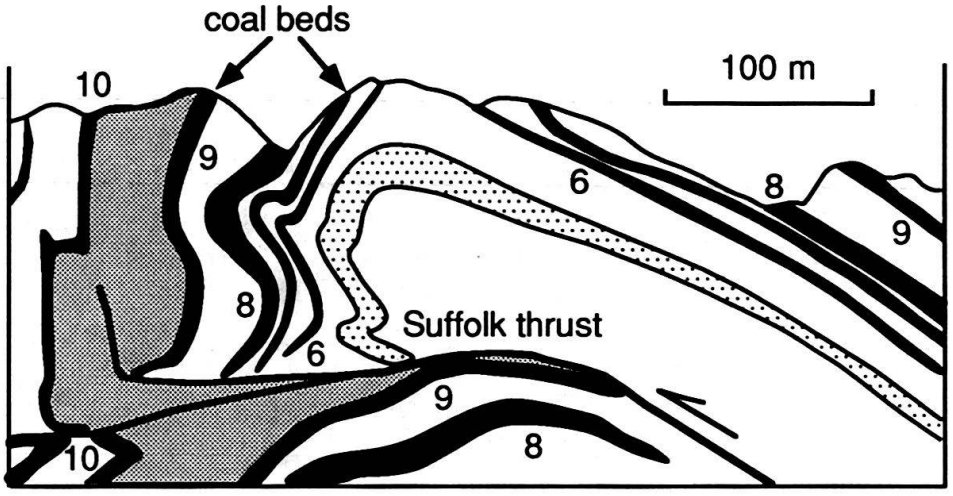

Fig. 5. Anticline in hanging wall of the Suffolk thrust of the anthracite coal basin, Pennsylvania Appalachians; cross section based on coal-mine mapping, with coal beds numbered (after Danilchik et al. 1955). Note the decreasing slip toward the fault tip.

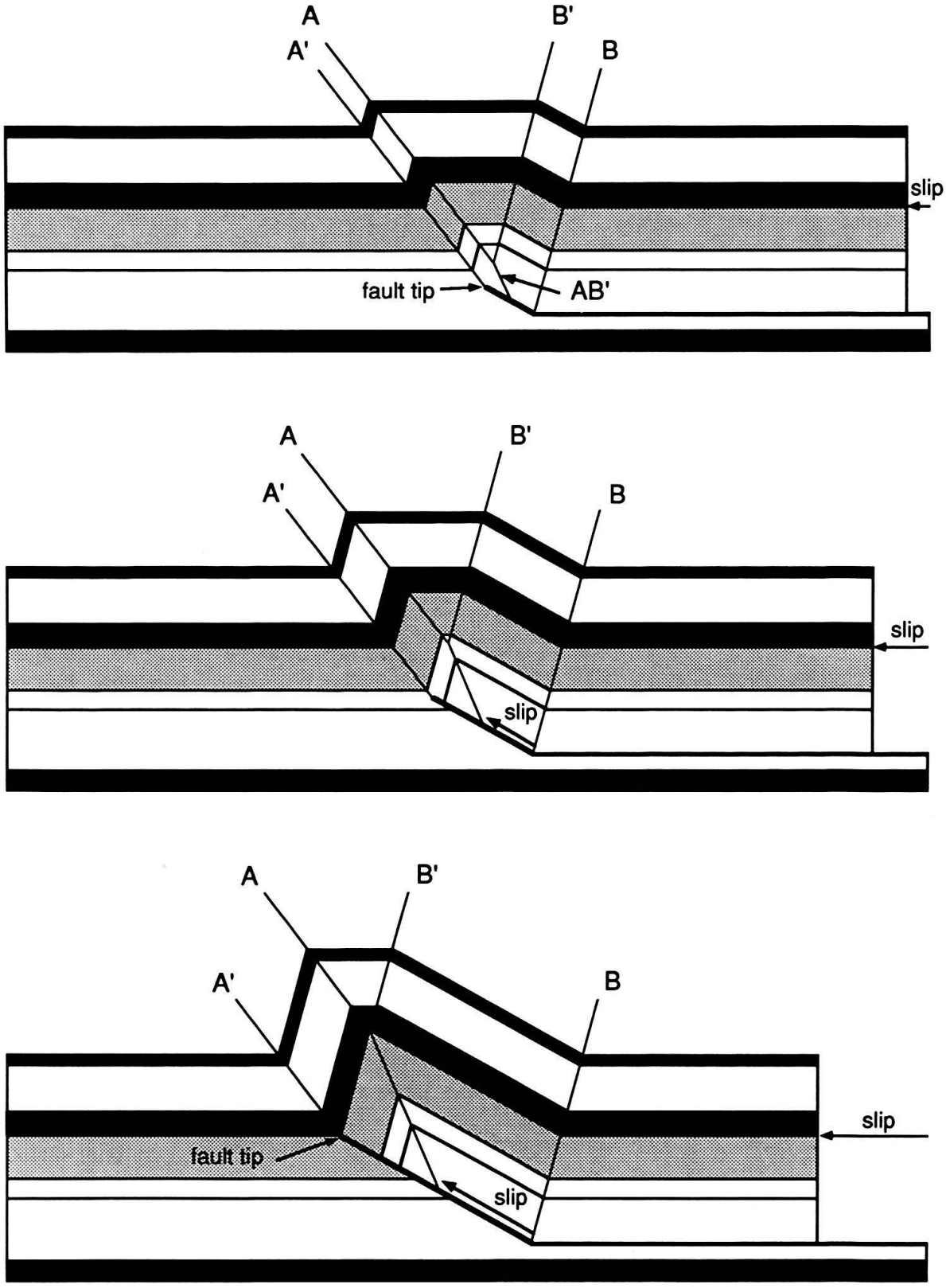

Fig. 6. Retrodeformable model of the progressive development of a simple-step fault-propagation fold (modified after Suppe 1983a and 1985, p. 351). The drawing is for a step-up angle of 29°, for which axial-surface *A* is fixed relative to the material. Under these conditions the constant-thickness and fixed-axis theories predict identical fold shapes.

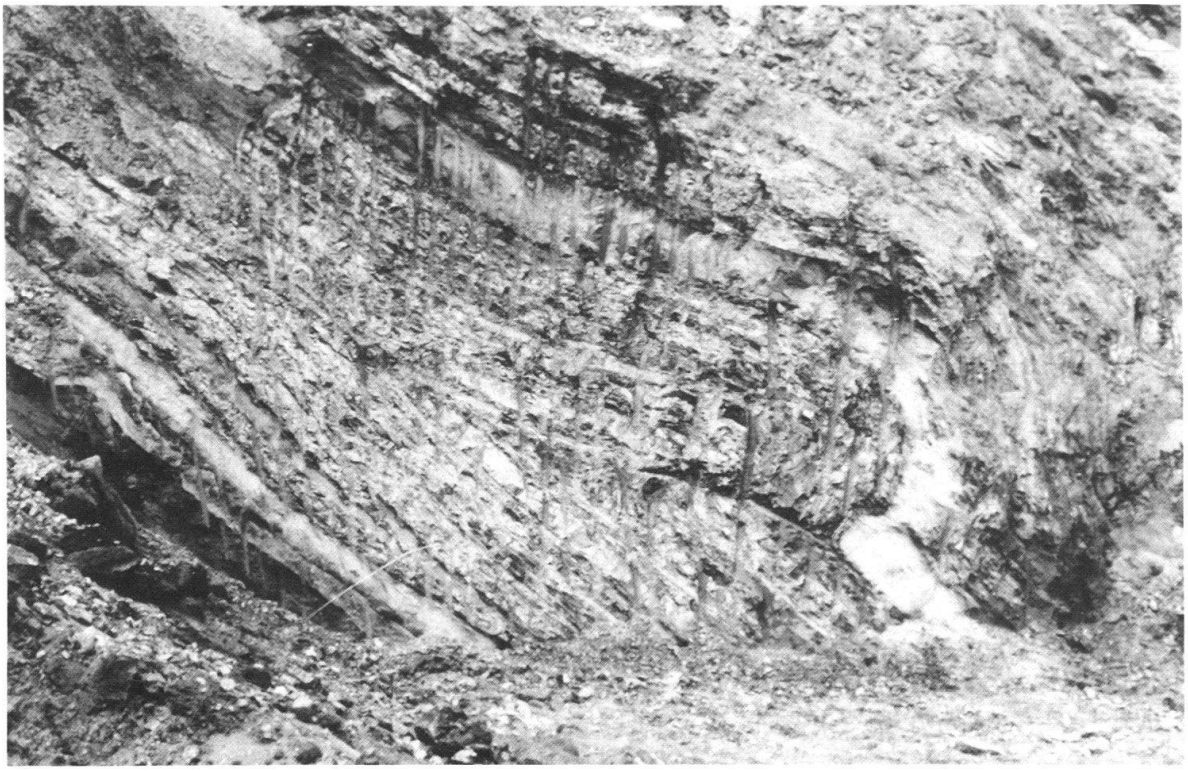

Fig. 7. Outcrop-scale fault-propagation fold in the Pleistocene Toukoushan Formation, Tsaochiao near Miaoli, western Taiwan overthrust belt. The entire structure has been tilted to the right in later map-scale folding. The thrust enters the upper left of the photograph along a decollement at the base of a thin sand bed, ramps stratigraphically upward, and finally terminates in the core of the syncline at the level of the thick sand bed at the lower right of the photograph. The origin of this structure by fault-propagation folding is recorded in the agreement of the anticlinal shape measured in the thin-bedded core of the fold ($\gamma^* \cong 33°$) and fault cut-off angles ($\Theta_1 = 0°$ and $\Theta_2 \cong 25°$) with the theoretical prediction of the constant-thickness theory [Fig. 17]. The height of the outcrop is about 3 meters.

thrust fault is just beginning to step up from its decollement, thereby forming two kink bands *A-A'* and *B-B'*. The middle and lower figures show the continued growth of the structure. Axial surface *A'* terminates at the fault tip; as the fault propagates, beds roll through axial surface *A'* from their flat-lying position into the steep kink band *A-A'*. Note that axial surface *AB'* branches at the same stratigraphic horizon as the fault tip, therefore it grows upward at the expense of axial surfaces *A* and *B'* as the fault propagates; for this reason it is labled *AB'*. Also note that axial surface *AB'* terminates at the fault where the hanging-wall thrust sheet changes from bedding parallel to cross cutting. Therefore axial surface *AB'* moves with the thrust sheet. In contrast axial surface *B* is pinned to the footwall, with the beds of the thrust sheet rolling through the axial surface; it is a fault-bend fold. Beds also roll through axial surface *B'* from the flat crest of the anticline into the back limb *B-B'* as axial surface *AB'* propagates. Axial surface *A* is fixed relative to the rock for the conditions of Figure 6; under other conditions it may move, as discussed below. The anticline grows self similarly as the fault tip propagates.

The essential geometric and kinematic features of the model fault-propagation fold (Fig. 6) that were just outlined are qualitatively matched by many actual examples.

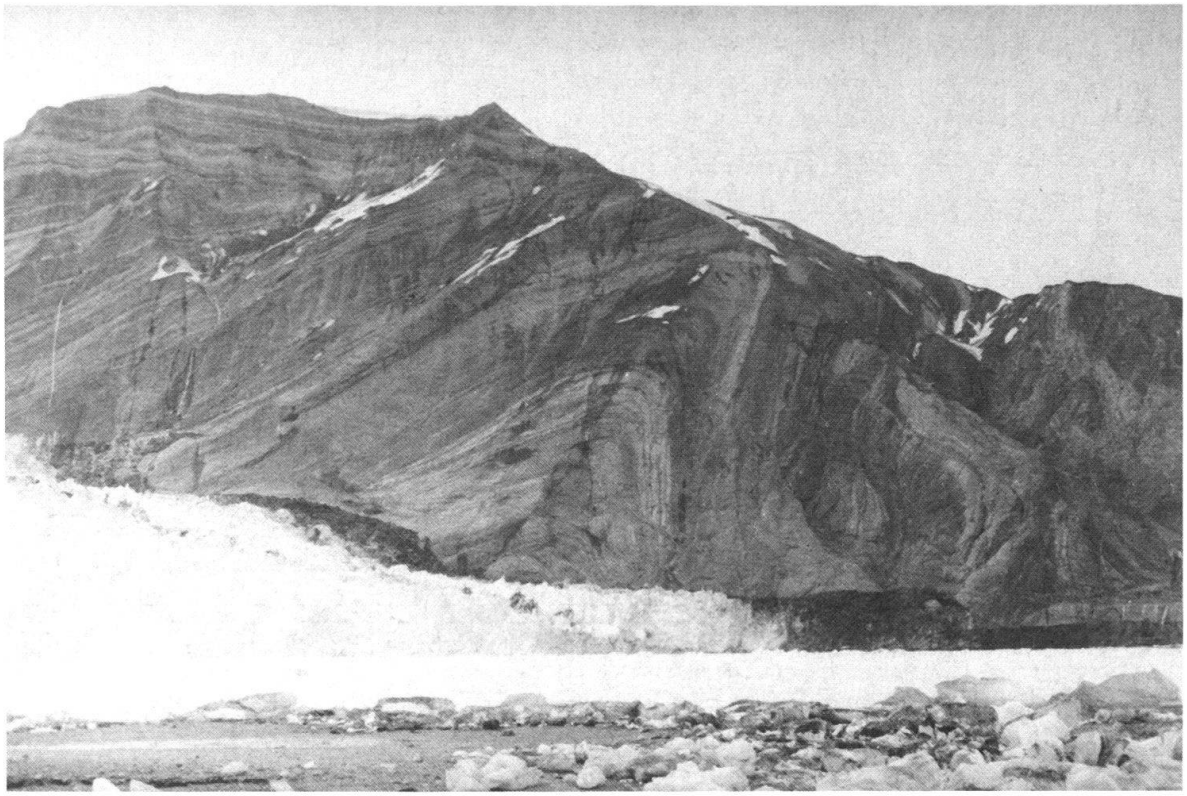

Fig. 8. Photograph of Yakataga anticline, Icy Bay, Gulf of Alaska. The thrust fault – recently exposed by the retreating glacier – terminates at the synclinal axial surface just to the left of the waterfall at the right edge of the photograph. The origin of this structure by fault-propagation folding is recorded in the agreement of the anticlinal shape measured in the thin-bedded core of the fold ($\gamma^* \cong 33°$) and fault cut-off angles ($\Theta_1 = 0°$ and $\Theta_2 \cong 23°$) with the theoretical prediction of the constant-thickness theory [Fig. 17].

Figure 7 is a photograph of an outcrop-scale fault-propagation fold – later tilted – from the western Taiwan overthrust belt. The thrust rides along a decollement at the base of a thin sand bed, ramps upward, and finally terminates in the core of the syncline at the level of the thick sand bed. The fold is tight and overturned in the thin-bedded core but is open above the thick sand bed, in qualitative agreement with the branching of the anticlinal axial surface *AB'* at the stratigraphic level of the fault tip in the schematic model (Fig. 6). The shape of the anticline in the thin-bedded core – in relation to the fault shape – is in quantitative agreement with theoretical predictions of fault-propagation folding developed below, as discussed in the figure caption. A mountain-side example from the Gulf of Alaska is shown in Figure 8, in which the thrust fault terminating at the synclinal axial surface has only recently been exposed by the receding glacier. The shape of the anticline is in quantitative agreement with theoretical predictions of fault-propagation folding theory as discussed in the figure caption. A map-scale example from western Taiwan is shown in Figure 9 with the fault terminating at the synclinal axial surface and the back limb having the same dip as the fault. In each of these examples there is qualitative agreement between the model and the natural fault-propagation folds.

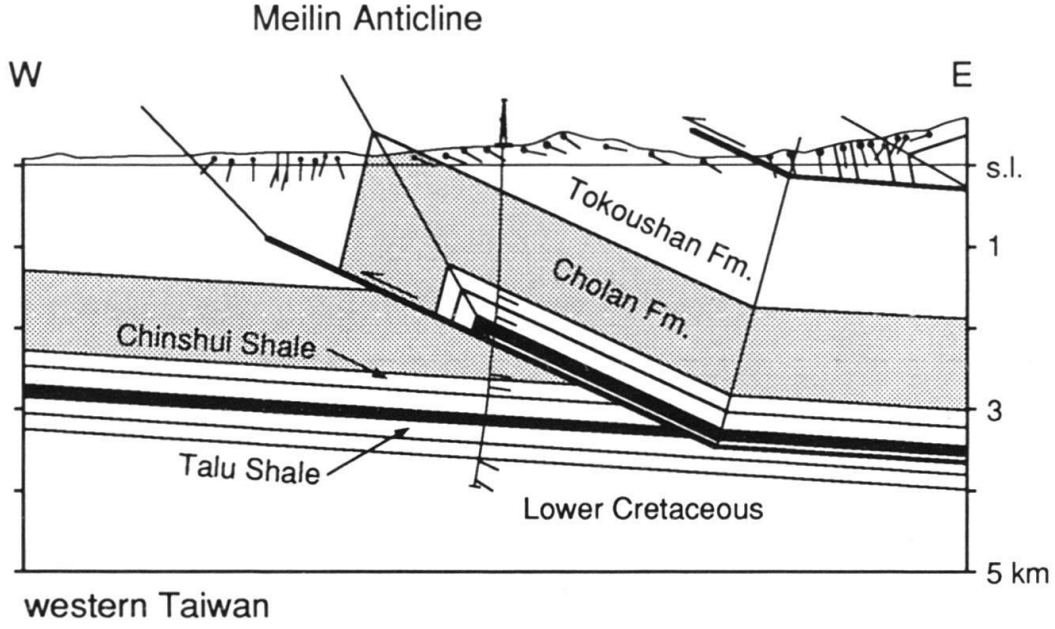

Fig. 9. Cross-section of Meilin anticline, western Taiwan overthrust belt near Chiayi, a fault-propagation fold similar to the schematic diagram of Figure 6. Cross-section is based on fixed-axis theory (modified after Suppe 1986).

2.2 Breaking through of fault-propagation folds

The thrust fault may continue to propagate self similarly (Fig. 6) all the way to the surface, leaving little obvious trace of its mode of propagation after erosion. Nevertheless some record of its origin by fault-propagation folding may be preserved. For example, the Naga thrust of northeastern India (Fig. 10) has propagated to the surface, yet the shape of the hanging-wall Digboi anticline shows that the thrust propagated as a fault-propagation fold based on its quantitative agreement with theoretical predictions, as discussed in the figure caption. However, with much more slip and erosion the hanging-wall anticline would be gone. Similarly the small fragments of tight to overturned synclines in the footwall of Figure 7 record the folding mode of propagation.

The self-similar mode of fault-propagation (Fig. 6) may be halted at any instant, as controlled by rock properties. Some formations may form tight folds more easily than others. For example in the outcrop example of Figure 7 the thrust tip was halted at a thick sandstone bed. In other cases the deformation is known to continue but not in the self-similar mode. The folding ceases and the fault breaks through the structure in a fracture mode. A number of situations are possible, as discussed in the following paragraphs with the help of balanced structural models and geologic examples.

2.2.1 Decollement breakthrough

If the fault tip encounters a weak stratum it may propagate along the bed as a decollement, as shown in Figures 11a and b, rather than continue propagating in the folding mode. In this case the fold ceases to grow and simply is translated with the thrust sheet. Decollement breakthrough also produces some fault-bend distortion of the fold, such

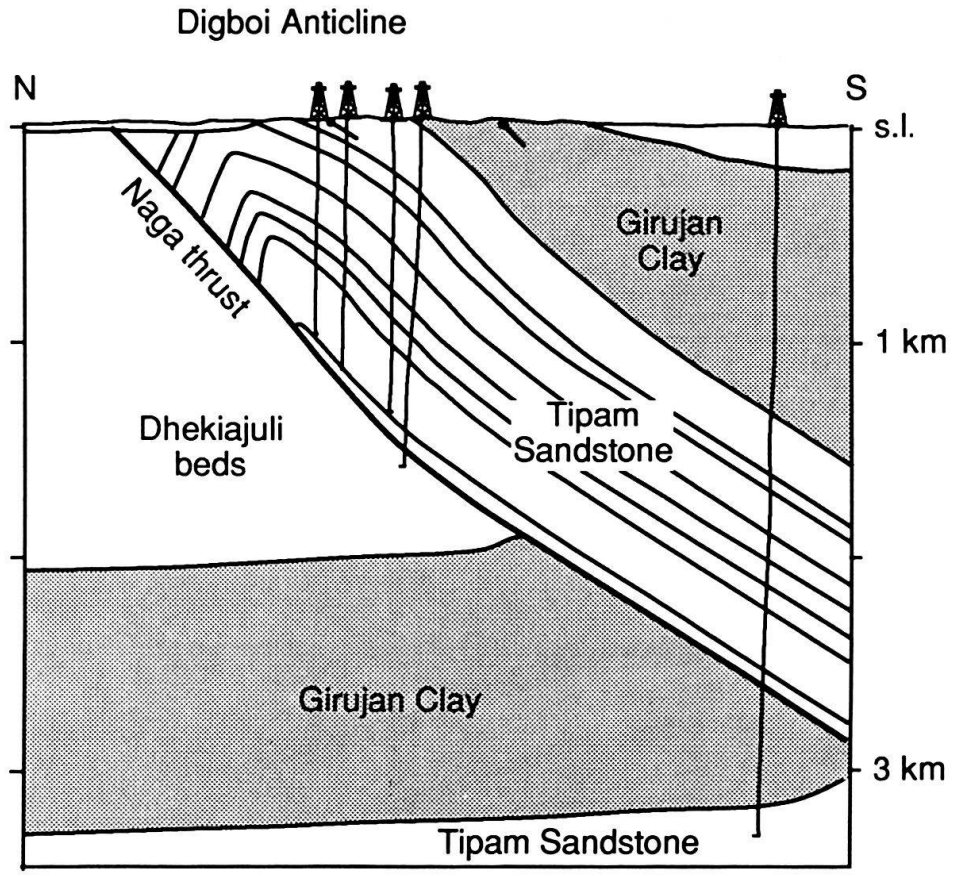

Fig. 10. Digboi anticline in the hanging wall of the Naga thrust, Naga Hills, northeast India (after MATHUR & EVANS 1964). The origin of this structure by fault-propagation folding is recorded in the agreement of the anticlinal shape ($\gamma^* = 40–45°$) and fault cut-off angles ($\Theta_1 = 0°$ and $\Theta_2 \cong 37°$) with the theoretical prediction of the constant-thickness theory for the special case of stepping up from a decollement ($\Theta_1 = 0°$ and $\Phi = \Theta_2$) [Fig. 17].

as kink bands *D-D'* and *E-E'* in Figures 11a and b. Ryckman Creek and Anschutz Ranch anticlines of the Absaroka thrust sheet in the Wyoming overthrust belt are examples of decollement breakthrough with large subsequent fault slip (Fig. 12). Akmagolik Creek anticline shows both decollement breakthrough and later amplification of the anticline by bedding slip (Fig. 1).

2.2.2 Synclinal, anticlinal, and steep-limb breakthrough

If the fault tip encounters layers that are unable to fold in the prescribed manner – in particular it may be unable to form the tight anticline *AB'* (Fig. 6) – the fold may lock and then fracture as stress builds up. Possible sites of breakthrough (Fig. 11) are along: (1) the synclinal axial surface *A'*, (2) the anticlinal axial surfaces *A* and *AB'*, or (3) somewhere within the steep limb, because these are the sites of most extensive pre-existing fractures. As slip on the new fault segment proceeds, a set of characteristic and distinctive fault-bend folds is produced (Fig. 11). Synclinal breakthrough produces the characteristic "snakehead" anticline on the hanging wall of a lystric thrust fault (Fig. 11c), anticlinal breakthrough produces the common tight to overturned syncline

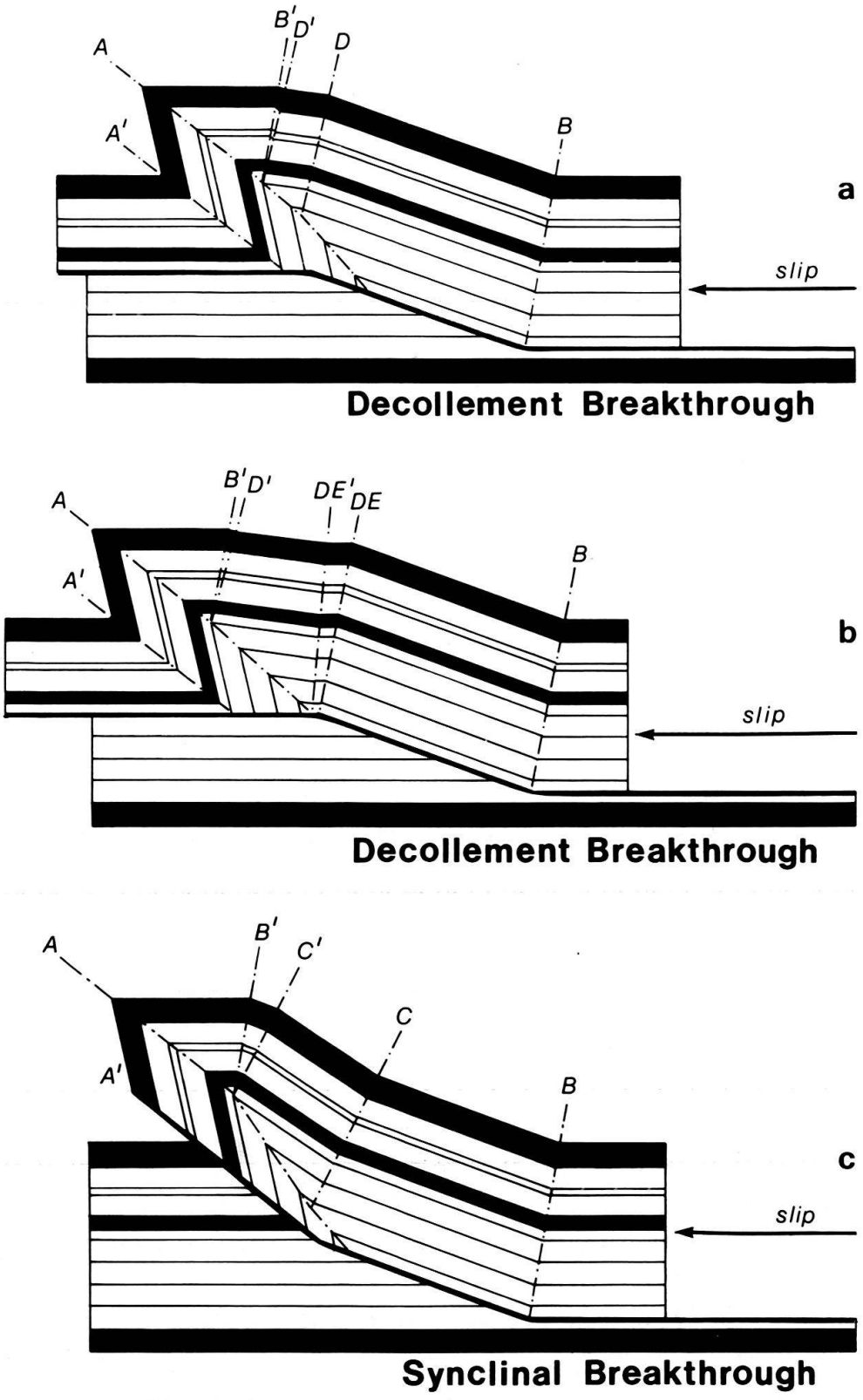

Fig. 11. Balanced structural models showing some possible types of breakthrough structures, (a and b) decollement breakthrough, (c) synclinal breakthrough, (d) anticlinal breakthrough, (e) high-angle or steep-limb breakthrough, and (f) low-angle breakthrough. Models were constructed assuming layer-parallel slip and preexisting axial surfaces locked in material.

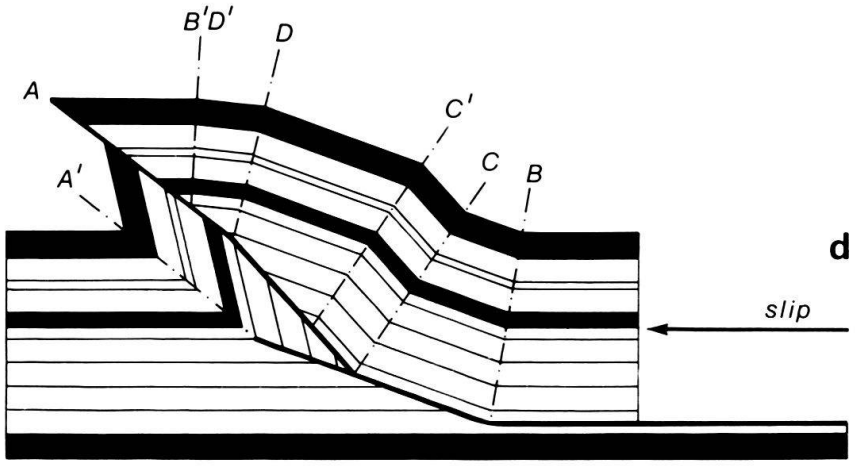

Anticlinal Breakthrough

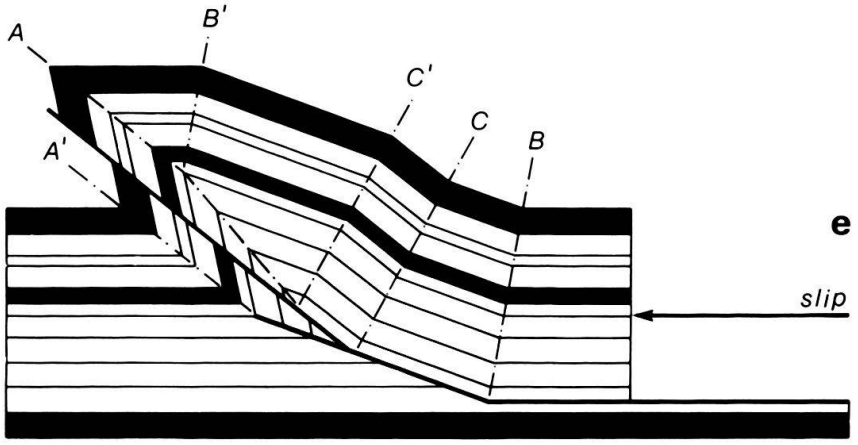

High-Angle Breakthrough

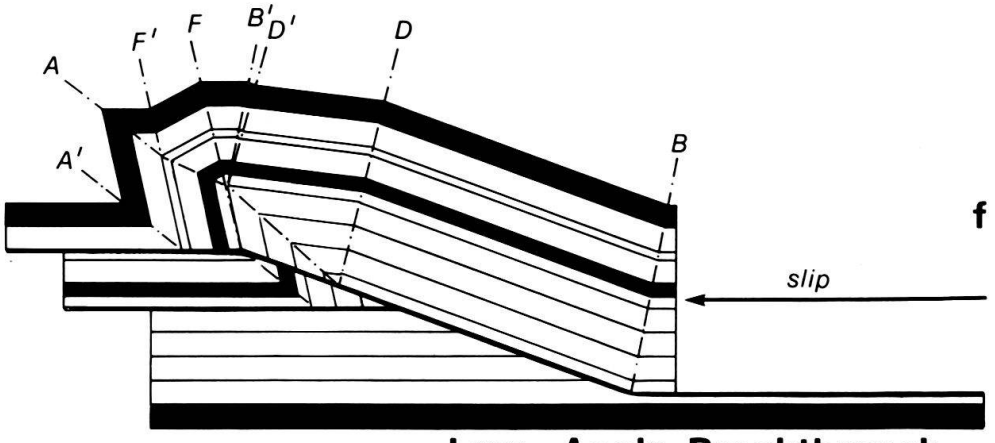

Low-Angle Breakthrough

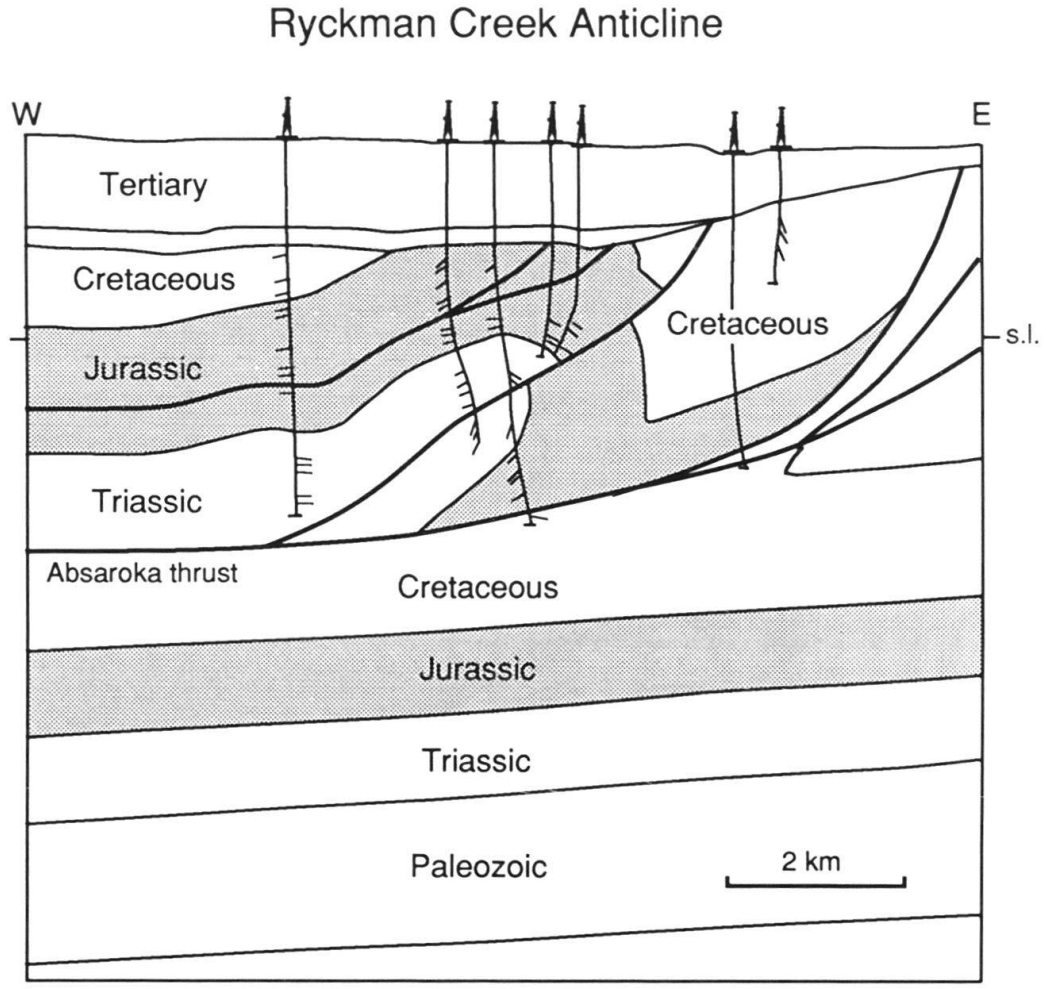

Fig. 12. Cross section of decollement breakthrough structure in the Absaroka thrust sheet, Ryckman Creek anticline, western U.S. overthrust belt, Wyoming (after LAMERSON 1982). Compare Figure 11b.

in the footwall with the axial surface approximately parallel to the thrust (Fig. 11d), and breakthrough within the steep limb combines all these features (Fig. 11e). A more complex example of a combined synclinal and steep-limb breakthrough along the Taipei thrust in western Taiwan is shown in Figure 13.

2.2.3 Low-angle and complex breakthrough

There is a natural tendency for breakthrough structures to become complicated. Even the examples of Figures 12 and 13 are more complex than the structural models of Figure 11. It is particularly common for the thrust to breakthrough at an angle that is less than the dips of the synclinal and anticlinal axial surfaces; one model is shown in Figure 11f. The thrust propagates at an angle that is close to the normal angle of thrust propagation within the overthrust belt, which is lower than the dips of the axial surfaces. A slightly more complicated but similar actual example is shown in Figure 14. Still other kinds of complex breakthrough are known to exist or may be envisaged; an example from western Taiwan is shown in Figure 15.

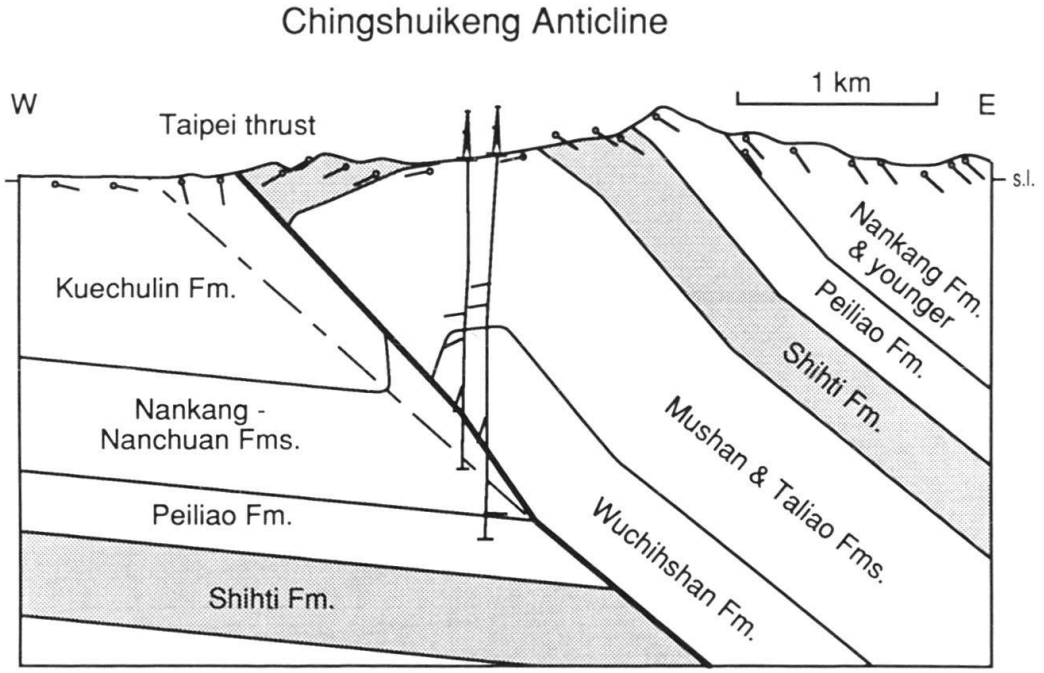

Fig. 13. Cross section steep-limb breakthrough of the Taipei thrust, Chingshuikeng anticline, western Taiwan overthrust belt (modified after SUPPE 1985, p. 352). The lowest fault segment shown is parallel to and aligned with the synclinal axial surface; it is therefore a synclinal breakthrough. Just to the east of the wells the thrust changes to a steep-limb or high-angle breakthrough, as recorded by the hanging-wall syncline that is observed in the surface dips.

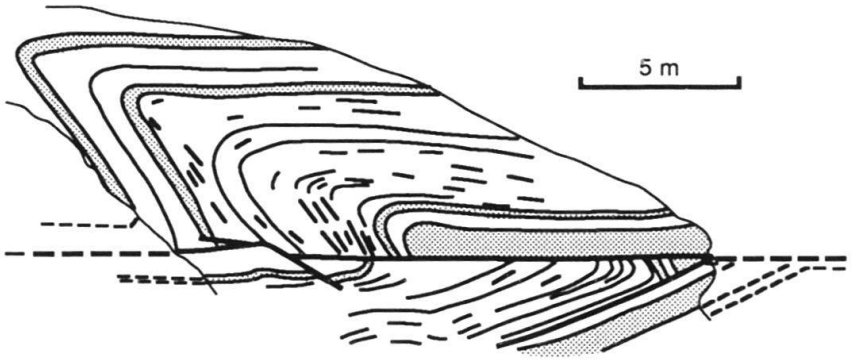

Fig. 14. Example of a low-angle breakthrough somewhat similar to the model of Figure 12e, Hope's Nose, Devon (after WILLIAMS & CHAPMAN 1983). The origin of this structure by fault-propagation folding is recorded in the agreement of the anticlinal shape and fault cut-off angles with the theoretical prediction of the constant-thickness theory for the special case of stepping up from a decollement ($\Theta_1 = 0°$ and $\Phi = \Theta_2$) [Fig. 17] ($\gamma^* \cong 31°$, $\Theta_1 = 0°$ and $\Theta_2 = 23°$ in the present deformed footwall state, which unfolds to $\Theta_2 = 20°$ according to fault-bend folding theory (SUPPE 1983b)).

The concept of breakthrough of fault-propagation folds thus provides qualitative explanation of a wide variety of asymmetric folding adjacent to thrust faults. Furthermore, in the cases of Figures 10 and 14, enough is known of the shapes to show that they are also in quantitative agreement with the following fault-propagation fold theory, as discussed in the figure captions.

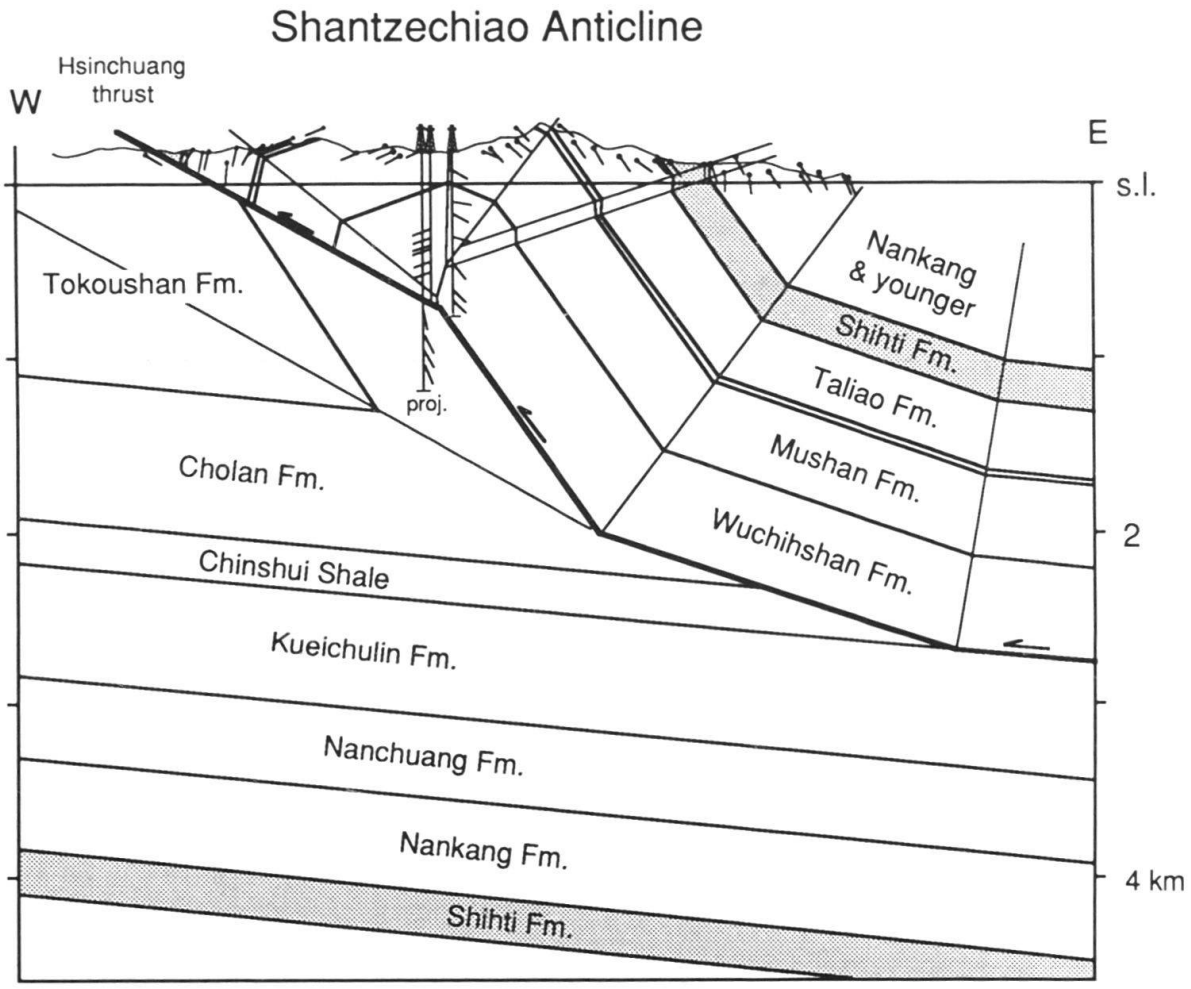

Fig. 15. Example of a complex breakthrough, Schantzechiao anticline, western Taiwan overthrust belt (modified after SUPPE 1980). The hanging-wall anticline and footwall syncline are fragments of different fault-propagation folds, formed on different ramps of the same thrust sheet.

3. Quantitative models of fault-propagation folding

It is possible to derive quantitative geometric relationships between fault shape and fold shape for the fault-propagation folding mechanism in a way that is quite analogous to the theory previously developed for fault-bend folding (SUPPE 1983b), which assumed conservation of layer thickness and bed length. These assumptions are commonly appropriate for brittle compressive folding; but in fact these assumptions may not be satisfied in the steep limbs of fault-propagation folds because of the extreme deformation. Nevertheless we develop the theory in the following section because of its well-defined end-member properties and because it seems to be a good approximation to some actual structures. Theories that allow thinning or thickening of the steep limb also are possible and one is explored in a later section. One value of these theories is that they provide a rigorous understanding of the implications of particular kinematic hypotheses. Furthermore, we may test the geological applicability of these theories by making appropriate measurements of the shapes of actual folds, which we do in a following section.

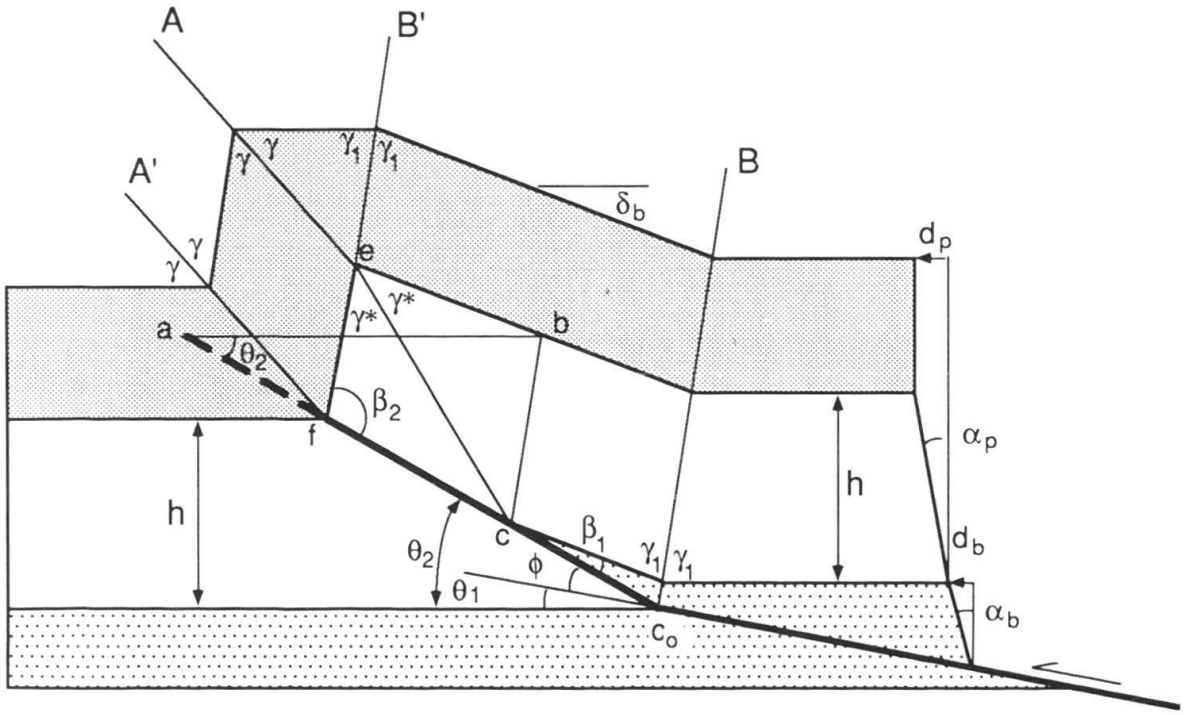

Fig. 16. Schematic drawing of general angular parallel fault-propagation fold showing the quantities used in the derivation of equations [1] through [8] describing the geometry and kinematics of constant-thickness fault-propagation folding (after SUPPE 1983a).

3.1 Constant-thickness fault-propagation folding

We now proceed to derive a general relationship between fold shape γ^* and fault shape Θ_1 and Φ (Fig. 16) for constant-thickness (parallel) fault-propagation folding, assuming angular hinges and conservation of bed length (SUPPE 1983a). The general assumptions and approach are the same as the theory of fault-bend folding (SUPPE 1983b). Note in Figure 16 that fault-propagation folding of this type requires a concave fault-bend Φ in the footwall, producing a synclinal fault-bend fold γ_1 downdip from the fault-propagation fold γ^*. We allow the possibility of a layer-parallel simple shear $S_p = \tan \alpha_p$ within the stratigraphic interval between hanging-wall cutoff c and the fault termination f. An additional shear $S_b = \tan \alpha_b$ is possible within the stratigraphic interval between hanging-wall cutoff c and footwall cutoff c_o because of the synclinal fault-bend fold (SUPPE 1983b). All axial surfaces bisect the angles between limbs, which is the condition for conservation of layer thickness (parallel folding).

By conservation of bed length along the horizon of fault termination, which is a distance h stratigraphically above the fault-bend c_o, we have

$$ab + d_p = be + ef \qquad [1]$$

where d_p is the excess bed length caused by possible shear $S_p = \tan \alpha_p = d_p/h$. By the law of sines we have from triangle Δabc

$$ab = h \left[\frac{\sin (\gamma_1 - \beta_1)}{\sin \gamma_1 \sin \Theta_2} \right] \qquad [2]$$

from triangle Δbce

$$be = h\left[\frac{\sin(\gamma_1 - \gamma^*)}{\sin\gamma_1 \sin\gamma^*}\right] \quad [3]$$

and from triangle Δcef

$$ef = h\left[\frac{\sin(\gamma^* - \beta_1)}{\sin\gamma^* \sin(2\gamma^* - \beta_1)}\right] \quad [4]$$

Combining (1) through (4) we obtain

$$S_p = \left[\frac{\sin(\gamma_1 - \gamma^*)}{\sin\gamma_1 \sin\gamma^*} + \frac{\sin(\gamma^* - \beta_1)}{\sin\gamma^* \sin(2\gamma^* - \beta_1)} - \frac{\sin(\gamma_1 - \beta_1)}{\sin\gamma_1 \sin\Theta_2}\right] \quad [5]$$

and

$$\sin\Theta_2 = \left[\frac{\sin\gamma^* \sin(\gamma_1 - \beta_1)}{\sin(\gamma_1 - \gamma^*) + \left[\frac{\sin\gamma_1 \sin(\gamma^* - \beta_1)}{\sin(2\gamma^* - \beta_1)}\right] - S_p \sin\gamma^* \sin\gamma_1}\right] \quad [6]$$

which is the fundamental equation of angular parallel fault-propagation folding. Two additional useful equations are

$$\gamma = 90° + \gamma^* - \gamma_1 \quad [7]$$

and

$$\beta_2 = 180° - 2\gamma^* + \beta_1 \quad [8]$$

In order to compute the shape of the fault-propagation fold γ^* produced by a given fault shape Θ_1 and Φ, we must first compute the shape of the back syncline γ_1, which is a fault-bend fold, by using the equations of angular parallel fault-bend folding (equation 9 corrects an error in equation 31, Suppe 1983b)[3])

$$\tan\Phi = \left[\frac{-\sin(\gamma_1 + \Theta_1)[\sin(2\gamma_1 + \Theta_1) + \sin\Theta_1]}{\cos(\gamma_1 + \Theta_1)[\sin(2\gamma_1 + \Theta_1) + \sin\Theta_1] - \sin\gamma_1\left[1 + \frac{\sin\Theta_1 \sin\gamma_1 S_b}{\sin(\gamma_1 + \Theta_1)}\right]}\right] \quad [9]$$

where S_b is possible shear of the hanging-wall stratigraphy between cutoffs c and c_o, and

$$\beta_1 = \Theta_1 + \Phi - (180° - 2\gamma_1) = \Theta_2 - (180° - 2\gamma_1) \quad [10]$$

---

[3]) It should be noted that there is a difference in sign convention between the theories of fault-bend folding (Suppe 1983b) and fault-propagation folding:

Fault-bend folding	Fault-propagation folding
$\Theta_1 = -$	$\Theta_1 = +$
$\beta_1 = -$	$\beta_1 = +$
$\gamma_1 = +$	$\gamma_1 = +$
$\Phi = +$	$\Phi = +$

Equations [9] and [10] are written in the sign convention for fault-propagation folding.

The shape of a fault-propagation fold is computed as follows. Choosing a specific fault shape Φ, Θ_1, and $\Theta_2 = \Phi + \Theta_1$, we iteratively solved [9] for γ_1 using Newton's method. The final cutoff β_1 is then computed from [10]. The results of these computations are presented graphically in Figure 7 of SUPPE (1983b). The next major step is solving [5] iteratively for γ^*. Now that we know γ^*, γ_1, and β_1 for a specific fault shape Φ and Θ_1, γ may be computed from [7].

This sequence of iterative computations has been performed for the case of no shear ($S_p = S_b = 0$) and is presented as lines of constant Φ and Θ_1 on the graph of Θ_2 versus γ^* and γ (Figs. 17a and 17b). It is generally inconvenient to use the equations directly in the solution of practical problems of structural interpretation. The graph is much more convenient in assessing the range of possible solutions; for example, if the fold shape γ^* is known we may quickly assess the possible fault shapes Φ and Θ_2.

An additional parameter that is often easy to determine in map-scale fault-propagation folds is the angle δ_b between the back-limb dip and the original orientation of bedding. By inspection of Figure 16 we see that δ_b is related to the axial angles γ and γ^* by

$$\delta_b = 2(\gamma - \gamma^*) \qquad [11]$$

This angle can be used to estimate the fault-bend Φ for a simple undisrupted fault-propagation fold, as is shown in a later section. At usual step-up angles ($\Theta_2 < 45°$), the back dip is approximately equal to the fault bend $\delta_b \approx \Phi$. Thus we may use δ_b to estimate the fault-bend Φ, without knowing much about a structure.

The above theory of fault-propagation folding is for any fault shape Φ and Θ_1 and homogeneous shears $S_p = \tan \alpha_p$ and $S_b = \tan \alpha_b$, such that there is compression at the fault tip. However in some cases the associated fault-bend Φ is from a bedding plane decollement $\Theta_1 = 0$ to a cross-cutting thrust $\Phi = \Theta_2$. This is the case of *simple-step fault-propagation folding* (Fig. 6) by analogy with simple-step fault-bend folding (SUPPE 1983b). The fundamental equation of angular parallel fault-propagation folding [5] may be simplified using $\Theta_1 = 0$, $\gamma_1 = (90° - \Theta_2/2)$, and several trigonometric identities to obtain

$$S_p = \left[\frac{1 + 2\cos^2 \gamma^*}{\sin 2\gamma^*} + \frac{\cos \Theta_2 - 2}{\sin \Theta_2} \right] \qquad [12]$$

which is the fundamental equation of simple-step fault-propagation folding; its solution is plotted on Figure 17 as the line $\Phi = \Theta_2$.

We will discuss the properties of the above theory in detail in a later section. However we should note here, before developing the fixed axial-surface theory of the next section, that the angular constant-thickness theory has the property that the direction in which material rolls through the anticlinal axial surface A (Fig. 6) varies with fault angle Θ_2. At high fault angles material rolls from the crest to the front limb, whereas at low fault angles material rolls from the front limb onto the crest. This prediction of beds rolling from the steep or overturned front limb through axial-surface A up onto the flat top – while kinematically possible – may seem geologically unlikely, considering the undeformed nature of beds on the crest of the fold, for example in Figure 1. It is this difficulty, plus the thought that layer thickness might not be conserved in the steep limb even under upper-crustal brittle conditions, that motivates the following

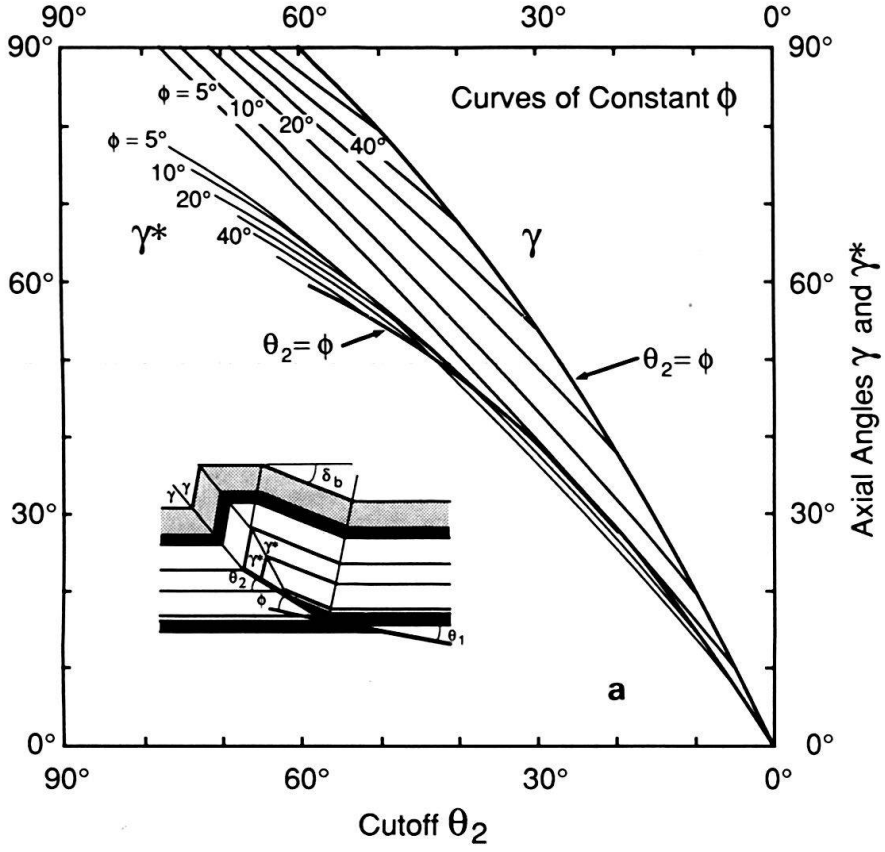
90°
60°
30°
0°
Curves of Constant ϕ
ϕ = 5°
10°
20°
40°
γ*
γ
θ2= ϕ
δb
θ1
a
Axial Angles γ and γ*
Cutoff θ2

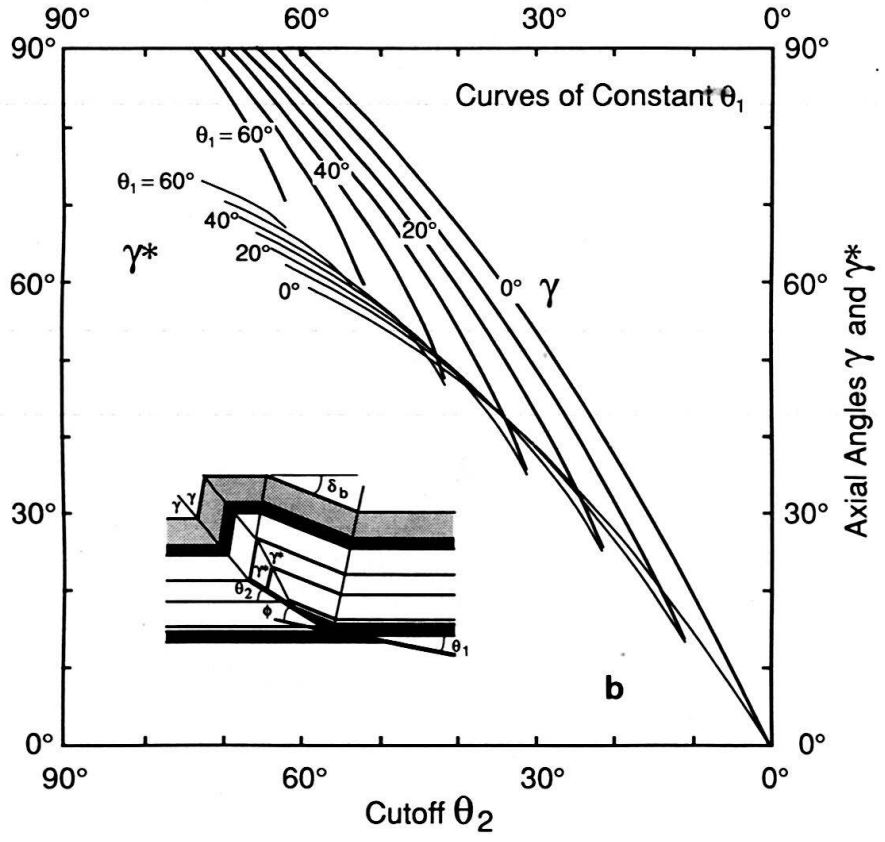
90°
60°
30°
0°
Curves of Constant θ1
θ1 = 60°
40°
20°
0°
γ*
γ
δb
θ1
b
Axial Angles γ and γ*
Cutoff θ2

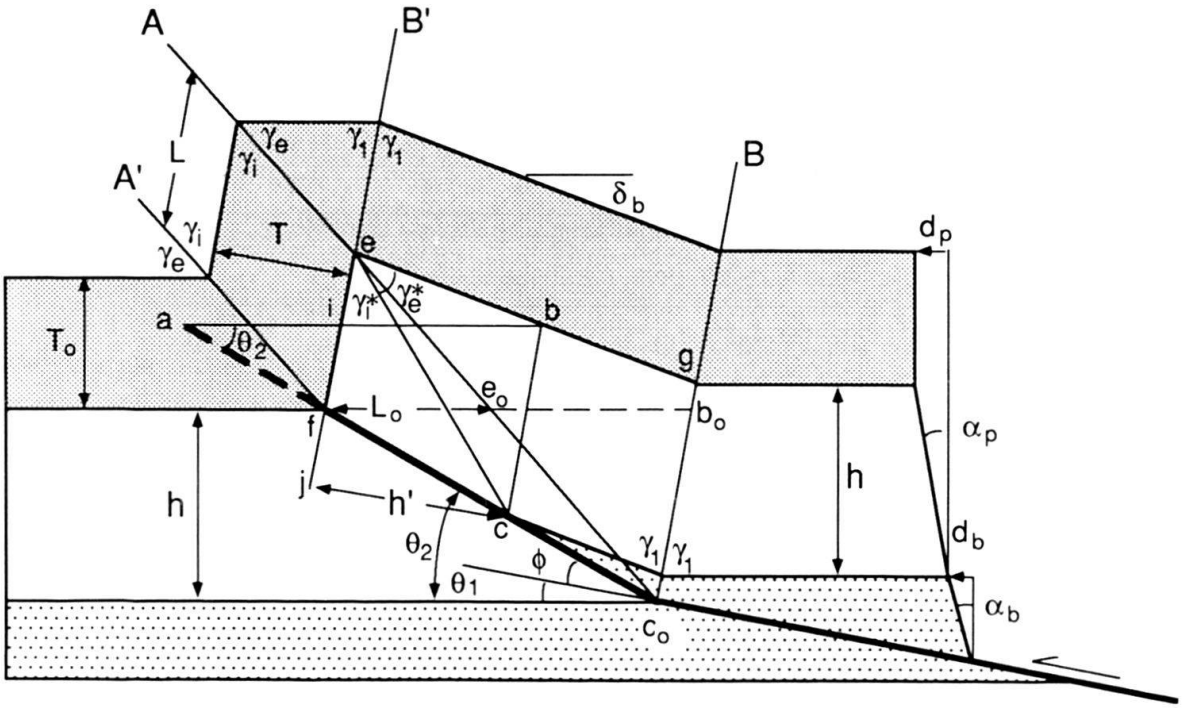

Fig. 18. Schematic drawing of general fault-propagation folding with a fixed anticlinal axial surface showing the quantities used in the derivation of equations [13] through [23].

slightly more complex theory. The back-limb kinematics are identical for the two theories.

3.2 Fault-propagation folding with fixed front anticlinal axial surface

Let us consider that it might not be mechanically possible for beds to roll through the front anticlinal axial surface A (Fig. 6), particularly with steeply dipping or overturned beds in the front limb (low cut-off angle Θ_2, as discussed above). Therefore we develop an alternative model of fault-propagation folding in which the anticlinal axial surface is locked in the material and the additional deformation that is required for structural continuity is confined to the steep limb where area – but not generally layer thickness or bed length – is conserved. The geometry of the fixed axial-surface problem is shown in Figure 18.

The equation for conservation of bed length [1], under the present model, is modified to

$$ab + d_p = be + ef\left[\frac{L_o}{L}\right] \qquad [13]$$

Fig. 17. Relationship between fault shape Θ_2 and fold shape γ and γ^* for constant-thickness fault-propagation folding based on equations [6], [7], [9], and [10], for no shear $S_b = S_p = 0$, a) with lines of constant fault-bend angle Φ, b) with lines of constant cut-off angle Θ_1. The special case of ramping from a decollement is shown as the lines $\Theta_2 = \Phi$, given by equation [12].

where L/L_o is the homogeneous stretch parallel to bedding in the front limb and L and L_o are the present and original bed lengths. As before, d_p is the excess bed length caused by a possible shear $S_p = \tan \alpha_p = d_p/h$ of the hanging-wall stratigraphy between cutoffs c and f.

The condition that the anticlinal axial surface A is fixed in the material allows [13] to be factored into two independent conditions, conservation of back-limb bed length

$$be = b_o e_o + d_p \quad [14]$$

and conservation of front-limb bed length

$$e_o f = ef\left[\frac{L_o}{L}\right] \quad [15]$$

The condition for continuity of layers across the axial surfaces is

$$\sin \gamma_e^* / \sin \gamma_i^* = T_o/T \quad [16a]$$

and

$$\sin \gamma_e / \sin \gamma_i = T_o/T \quad [16b]$$

where γ_e^*, γ_e, γ_i^*, and γ_i are external and internal axial angles and T_o and T are the external and internal layer thicknesses (Fig. 18). Combining [16] we obtain

$$\gamma_i = \sin^{-1}\left[\frac{\sin \gamma_i^* \sin \gamma_e}{\sin \gamma_e^*}\right] \quad [17]$$

The condition for conservation of area in the front limb is

$$L/L_o = T_o/T = \sin \gamma_e^* / \sin \gamma_i^* \quad [18]$$

From triangle Δbei

$$\gamma_i + \gamma_e = (180° - 2\gamma_1) + \gamma_i^* + \gamma_e^* \quad [19]$$

Combining [17] and [19] and rearranging we obtain

$$\gamma_i^* = \tan^{-1}\left[\frac{\sin(2\gamma_1 - \gamma_e^* + \gamma_e)}{[\sin \gamma_e / \sin \gamma_e^*] + \cos(2\gamma_1 - \gamma_e^* + \gamma_e)}\right] \quad [20]$$

Expanding [14] based on Figure 18

$$h[\cot \gamma_e^* - \cot \gamma_1] = h[\cot \gamma_e + \cot \gamma_1 + S_p] \quad [21]$$

and rearranging

$$\gamma_e = \cot^{-1}[\cot \gamma_e^* - 2 \cot \gamma_1 - S_p] \quad [22]$$

Expanding [15] based on Figure 18 and [18]

$$h\left[\frac{\sin(\gamma_e - \Theta_2)}{\sin \gamma_e \sin \Theta_2}\right] = h\left[\frac{\sin(\gamma_e + \gamma_i - \Theta_2 - \gamma_i^*)}{\sin \gamma_e^* \sin(\gamma_e + \gamma_i - \Theta_2)}\right]\left[\frac{\sin \gamma_i^*}{\sin \gamma_e^*}\right] \quad [23]$$

and rearranging

$$\left[\frac{\cot \gamma_i^* - \cot(\gamma_e + \gamma_i - \Theta_2)}{\cot \Theta_2 - \cot \gamma_e}\right] - \left[\frac{\sin^2 \gamma_e^*}{\sin^2 \gamma_i^*}\right] = 0 \quad [24]$$

By equating with [19], [20], and [22] it is possible to transform [24] into a form that is analogous to [6] for the constant-thickness theory, expressing γ_e^* as a function of γ_1, Θ_2, and S_p, however it is quite messy and unnecessary for numerical solution.

The shape of a fixed-axis fault-propagation fold (γ_e, γ_e^*, γ_i, γ_i^*, γ_1) as a function of fault shape (Φ, Θ_1, $\Theta_2 = \Phi + \Theta_1$) and shear ($S_p = \tan \alpha_p$, $S_b = \tan \alpha_b$) is defined by equations [9], [17], [20], [22], and [24]. We have solved them iteratively by Newton's method. Figures 19 and 20 are graphs of the solutions, for the case of no shear ($S_p = S_b = 0$), plotted on the coordinates Θ_2 versus γ_e, γ_e^*, γ_i and γ_i^* with curves of constant Φ, Θ_1 and $T_o/T = L/L_o$.

In addition to the general theory of fixed-axis fault-propagation folding, it is also useful to have the equation for the special case of stepping up from a decollement in which $\Theta_1 = 0°$ and $\Phi = \Theta_2$. This equation of simple-step fixed-axis fault-propagation folding may be obtained from [18], [22], and [23] using $\Theta_2 = 180° - 2\gamma_1$, $\gamma_1 = \gamma_i^* + \gamma_e^*$, and several trigonometric identities.

$$S_p = 2 \cot \gamma_e^* + \frac{2 \cos \Theta_2 - 3}{\sin \Theta_2} \qquad [25]$$

Its solution is plotted as part of Figure 19 and is labled $\Theta_1 = 0°$ or $\Phi = \Theta_2$.

4. Comparison and diagnostic testing of the constant-thickness and fixed-axis theories

The two relatively simple theories of fault-propagation folding that are derived above – one conserving layer thickness in the steep limb and the other fixing the anticlinal axial surface A – have produced a bewildering set of graphs that may seem too complex to apply easily to many practical problems of subsurface structural interpretation. In particular the number of angles specified in the fixed-axis theory is so large that we could only hope to observe them all on a map-scale structure under the most unusual and ideal circumstances. To fully test the theories we would have to observe not only the fault shape and the dips of beds, but also the orientations of axial surfaces because we can no longer assume that they bisect the angle between fold limbs.

Nevertheless it is important to realize that there are only two independent variables in each theory – the shape of the fault (Θ_1 and Θ_2). For this reason it seems possible to recast the theories in terms of several easily measured quantities that allow us to diagnose whether or not a given fold has a shape that is consistent with either theory of fault-propagation folding. If its shape is consistent, then we can use the graphs already presented to solve for the complete shape of the fold and fault.

We seek to recast the theories of fault-propagation folding in terms of easily measurable quantities that are diagnostic. What is easily measured of course varies from case to case, but in what follows we consider limb dips, widths, and heights to be most generally useful. Orientations of faults and axial surfaces are more commonly unknown.

Furthermore we consider only situations in which there is no excess shear ($S_p = S_b = 0$). It is our experience with fully constrained fault-bend folds that shear under brittle conditions is generally zero; we have observed only one possible exception to this generalization (Suppe 1984). In saying this we recognize that traditional methods of cross-section construction and line-length balancing commonly lead to sol-

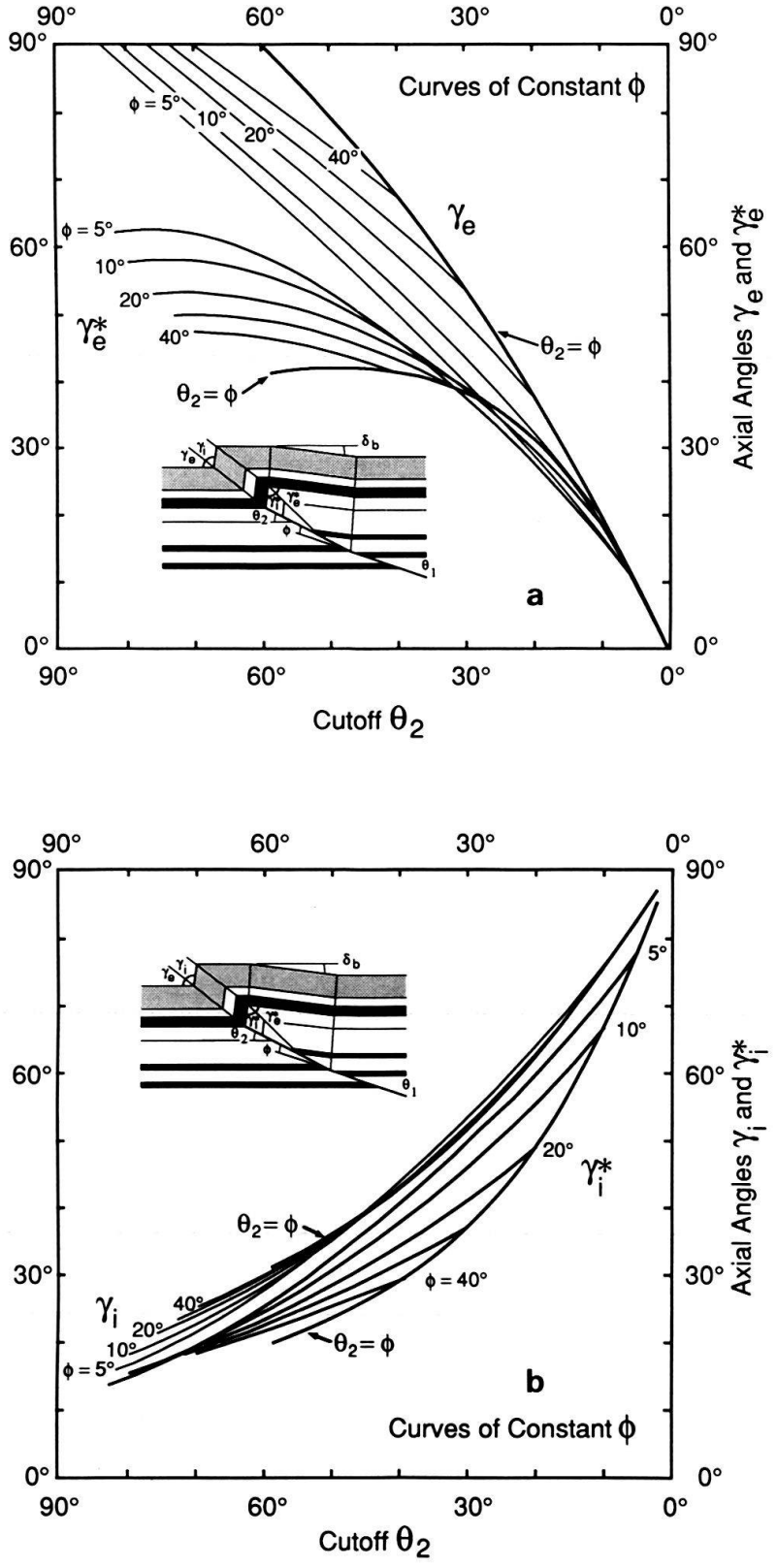

Fig. 19. Relationship between fault shape and fold shape for fixed-axis fault-propagation folding based on equations [9], [10], [20], [22], and [24], for no shear $S_b = S_p = 0$. Figures a) and b) present the external and internal angles γ_e, γ_e^*, γ_i and γ_i^* as a function of cut-off angle Θ_2 with curves of constant fault-bend Φ, whereas Figures c) and d) have curves of constant initial cut-off angle Θ_1.

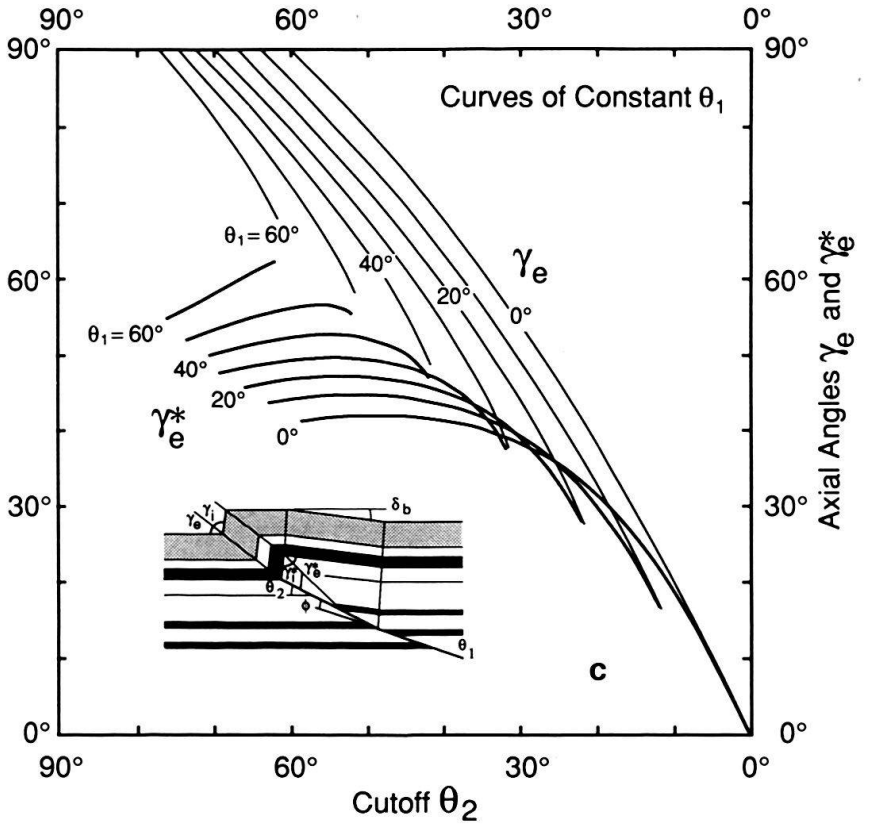
90°
60°
30°
0°
Curves of Constant θ_1
$\theta_1 = 60°$
40°
20°
0°
γ_e
γ_e^*
δ_b
θ_2
ϕ
θ_1
c
Axial Angles γ_e and γ_e^*
Cutoff θ_2

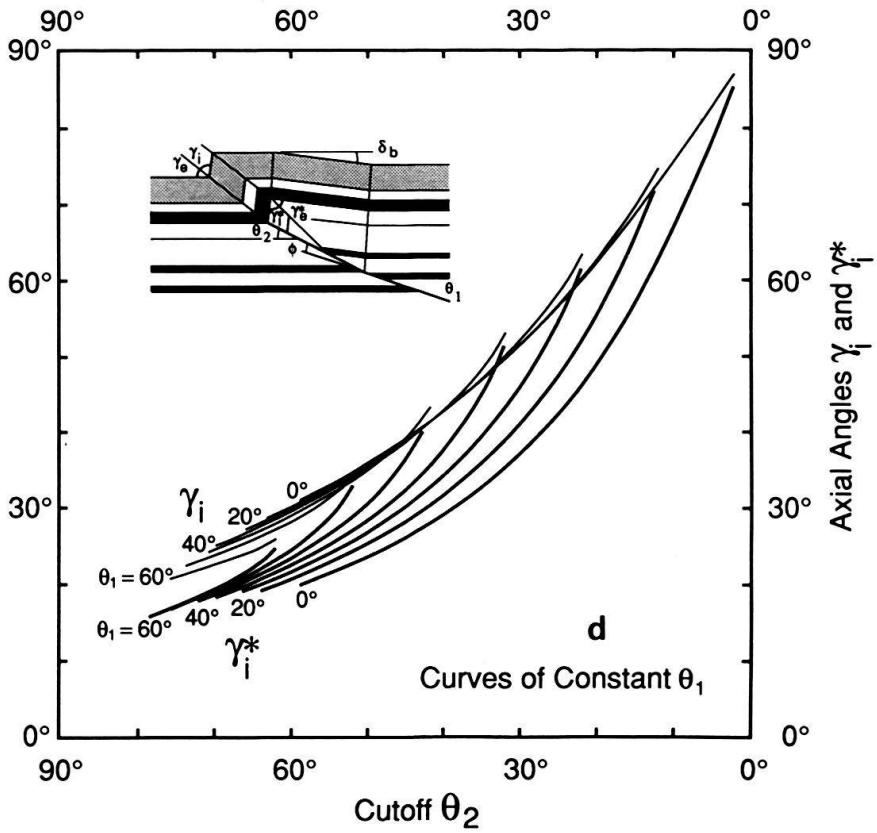
90°
60°
30°
0°
γ_i
γ_i^*
$\theta_1 = 60°$
40°
20°
0°
δ_b
θ_2
ϕ
θ_1
d
Curves of Constant θ_1
Axial Angles γ_i and γ_i^*
Cutoff θ_2

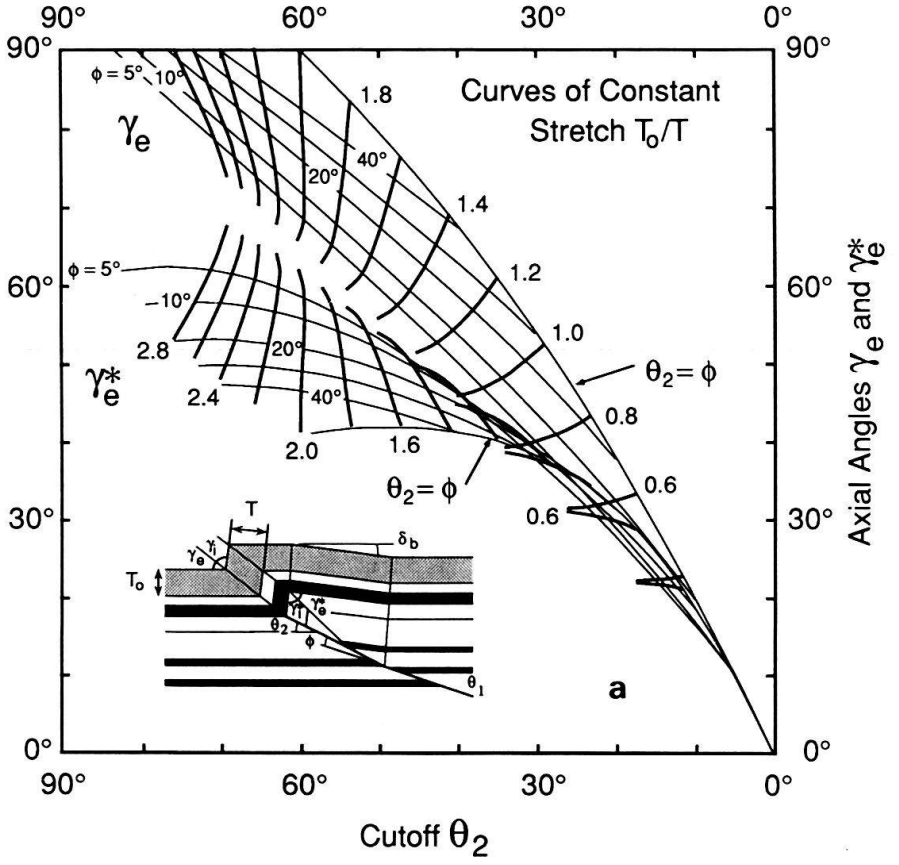
90°
60°
30°
0°
Curves of Constant
Stretch T_o/T
γ_e
γ_e^*
$\phi = 5°$
10°
20°
40°
1.8
1.4
1.2
1.0
0.8
0.6
2.8
2.4
2.0
1.6
$\theta_2 = \phi$
T
δ_b
T_o
θ_2
ϕ
θ_1
a
Cutoff θ_2
Axial Angles γ_e and γ_e^*

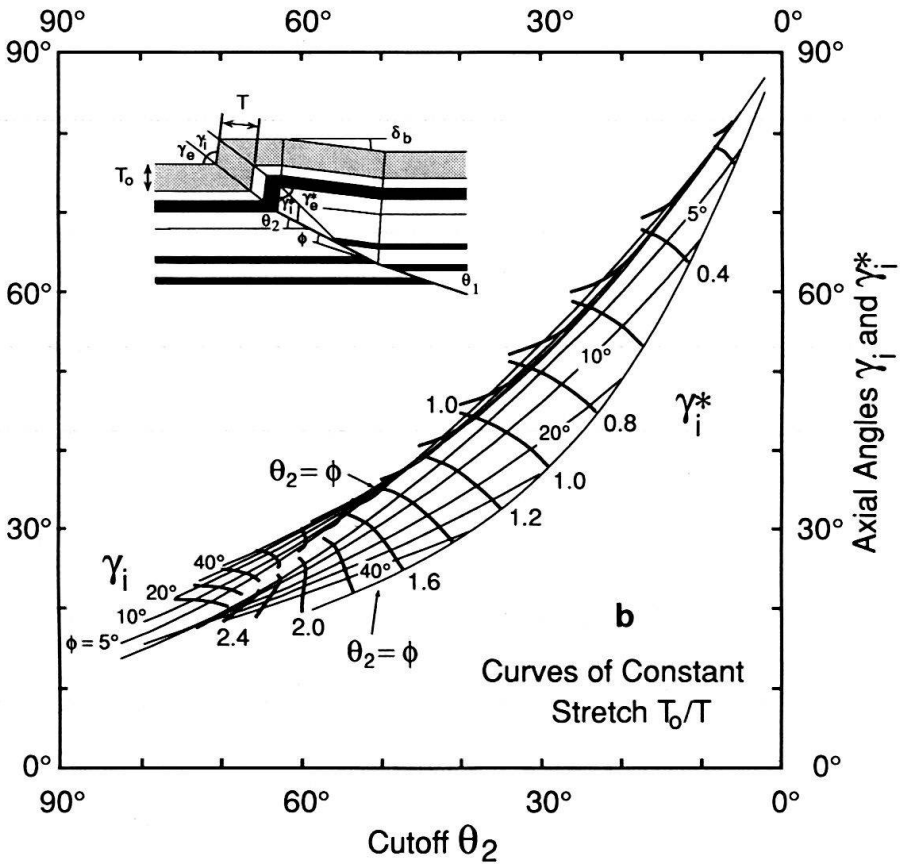
90°
60°
30°
0°
γ_i^*
γ_i
5°
10°
20°
40°
0.4
0.8
1.0
1.2
1.6
2.0
2.4
$\theta_2 = \phi$
T
δ_b
T_o
θ_2
ϕ
θ_1
b
Curves of Constant
Stretch T_o/T
Cutoff θ_2
Axial Angles γ_i and γ_i^*

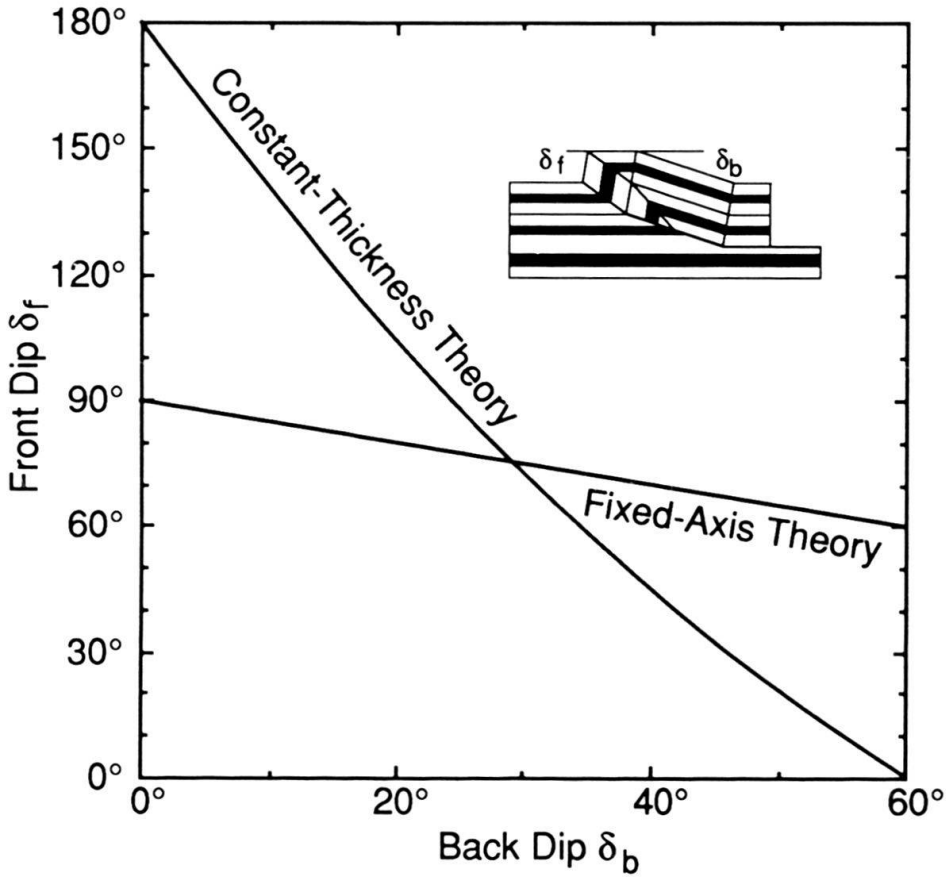

Fig. 21. A graph of the relationship between back-limb dip δ_b and front-limb dip δ_f for constant-thickness and fixed-axis fault-propagation folds in the case of thrusts stepping up from a decollement ($\Theta_2 = \Phi$). At step-up angles quite different from 29°, where they coincide, the two theories should be easily distinguished with data.

utions that involve non-zero shear, however such solutions are underconstrained (Woodward et al. 1985). Therefore we guess that shear is usually zero, which is the assumption of all the graphs in this paper. It is possible that shear is important in some structures; elsewhere we have considered the implications of shear within specific stratigraphically controlled intervals with possible application to sequences containing evaporites (Mosar & Suppe 1990).

4.1 Relationship between front δ_f and back dips δ_b

Let us begin our comparison and testing of the theories by considering that many fault-propagation folds will involve a thrust stepping up from a decollement. In this case the back dip δ_b – relative to the regional dip – is equal to the step-up angle $\delta_b = \Phi = \Theta_2$. Figure 21, which presents the combinations of front δ_f and back dips δ_b predicted by the two theories, shows us two things. First, the two theories only coincide at a step-up angle $\delta_b = \Phi = \Theta_2$ of 29°. Secondly, away from the 29° step-up angle the

Fig. 20. Layer-parallel stretch L/L_o or thickness ratio T_o/T within the front limb of fixed-axis fault-propagation folds as a function of cut-off angle Θ_2 and fold shape a) γ_e and γ_e^* and b) γ_i and γ_i^*. The fixed-axis theory coincides with the constant-thickness theory along the line $T_o/T = 1$.

two theories give quite different predictions. For example at a step-up angle of 20° a front limb dip δ_f of 80° is predicted for the fixed-axis theory whereas an overturned dip of 104° is predicted for the constant-thickness theory, a difference of 24°. This gives us optimism that we may be able to distinguish the two theories with data.

The 29° step-up angle at which the two theories coincide is the angle at which there is no thickening or thinning in the fixed-axis theory and no motion of the front-anticlinal axial surface A in the constant-thickness theory. We see in general in Figure 20 that the fixed-axis theory predicts thickening of the front limb $T_o/T<1$ at step-up angles Θ_2 less than about 29°, whereas thinning of the front limb $T_o/T>1$ is predicted at higher step-up angles. In the constant-thickness theory particles move from the steep front limb through axial-surface A onto the crest at step-up angles Θ_2 less than about 29°, whereas particles move from the crest into the front limb at higher step-up angles. In the general case ($\Theta_1 \geq 0°$) the two theories coincide along the line $T_o/T=1$ (Fig. 20).

Thus encouraged by Figure 21, we proceed to look at the relationship between front and back dips for the general case of all possible fault shapes ($\Theta_1 \geq 0°$), which is

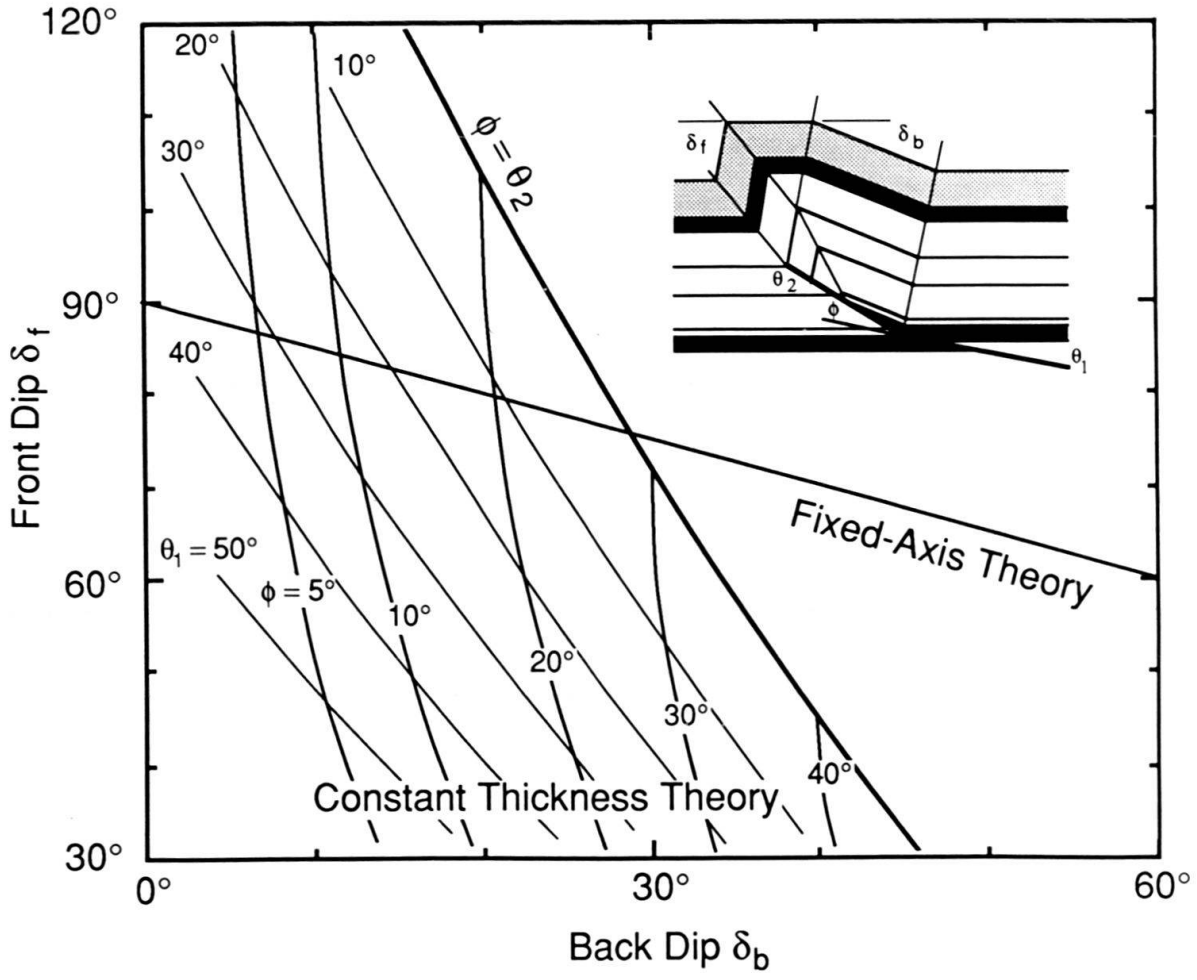

Fig. 22. A graph of the general relationship between back-limb dip δ_b and front-limb dip δ_f for constant-thickness and fixed-axis fault-propagation folds. The fixed-axis theory is represented by a single line (equation [26]) whereas the constant-thickness theory is represented by the area from the $\Phi = \Theta_2$ line to the left. Above the fixed-axis line beds move from the front limb onto the crest, whereas below the line beds move from the crest into the front limb.

given in Figure 22. As expected, what was a single line for the constant-thickness theory in Figure 21 has become a family of curves in the more general case. However it is perhaps surprising that the fixed-axis theory is still represented by a single line in the general case. The reason for this is that the front-limb dip δ_f must be parallel to the back axial surfaces B and B' because axial surface A is fixed, therefore

$$\delta_f = \gamma_1 = (180° - \delta_b)/2 \qquad \text{(fixed-axis theory)} \qquad [26]$$

Thus only one piece of information is contained in limb dips in the fixed-axis theory, whereas these two dips fully constrain the fault shape in the constant-thickness theory. Additional information on the fault shape for the fixed-axis theory is contained in either the ratios of limb widths (W_f/W_b) or heights (H_b/H_f), which are derived as follows.

4.2 Ratios of limb widths (W_f/W_b) and heights (H_b/H_f)

4.2.1 Fixed-axis theory

It can be shown from triangle $\Delta e_o c_o f$ in Figure 18, the law of sines, and equations [16], [18], and [23] that the front-limb width W_f is

$$W_f = e_o f = ef\left[\frac{\sin\gamma_i}{\sin\gamma_e}\right] = h\left[\frac{\sin(\gamma_e - \Theta_2)}{\sin\gamma_e \sin\Theta_2}\right] \qquad [27]$$

Because the back-limb width W_b and the line eg are two sides of an isosoles triangle, this width can be expressed as

$$W_b = eb + bg$$

where eb is

$$eb = h[\cot\gamma_e^* - \cot\gamma_1]$$

based on triangle Δebc and bg is

$$bg = (fc_o - fc)\left[\frac{\sin(\gamma_1 + \Theta_2)}{\sin\gamma_1}\right] = h\left[\frac{1}{\sin\Theta_2} - \frac{\sin\gamma_i/\sin\gamma_e}{\sin(\gamma_e + \gamma_i - \Theta_2)}\right]\left[\frac{\sin(\gamma_1 + \Theta_2)}{\sin\gamma_1}\right]$$

by its relationship to the fault slip $c_o c$. Combining we have the back-limb width W_b as

$$W_b = h[\cot\gamma_e^* - \cot\gamma_1] + h\left[\frac{1}{\sin\Theta_2} - \frac{\sin\gamma_i/\sin\gamma_e}{\sin(\gamma_e + \gamma_i - \Theta_2)}\right]\left[\frac{\sin(\gamma_1 + \Theta_2)}{\sin\gamma_1}\right] \qquad [28]$$

Combining [27] and [28] we obtain the ratio of limb widths

$$\left[\frac{W_f}{W_b}\right] = \left[\frac{\left[\dfrac{\sin(\gamma_e - \Theta_2)}{\sin\gamma_e \sin\Theta_2}\right]}{[\cot\gamma_e^* - \cot\gamma_1] + \left[\dfrac{1}{\sin\Theta_2} - \dfrac{\sin\gamma_i/\sin\gamma_e}{\sin(\gamma_e + \gamma_i - \Theta_2)}\right]\left[\dfrac{\sin(\gamma_1 + \Theta_2)}{\sin\gamma_1}\right]}\right] \qquad [29]$$

The backlimb height is simply

$$H_b = W_b \sin \delta_b = W_b \sin (2\,\gamma_1) \qquad [30]$$

From [27] we have

$$ef = W_f \left[\frac{\sin \gamma_e}{\sin \gamma_i} \right]$$

also using [26] $\sin \delta_f = H_f/ef = \sin (\gamma_i + \gamma_e) = \sin \gamma_1$

yielding the front-limb height

$$H_f = W_f \sin (\gamma_i + \gamma_e) \left[\frac{\sin \gamma_e}{\sin \gamma_i} \right] = W_f \sin \gamma_1 \left[\frac{\sin \gamma_e}{\sin \gamma_i} \right] \qquad [31]$$

Finally, combining [30] and [31] we have the ratio of limb heights

$$\left[\frac{H_b}{H_f} \right] = \left[\frac{W_b}{W_f} \right] \left[\frac{\sin (2\,\gamma_1)}{\sin (\gamma_i + \gamma_e) \left[\frac{\sin \gamma_e}{\sin \gamma_i} \right]} \right] = \left[\frac{W_b}{W_f} \right] \left[\frac{2 \cos \gamma_1 \sin \gamma_i}{\sin \gamma_e} \right] \qquad [32]$$

4.2.2 Constant-thickness theory

The corresponding width and height ratios for the constant-thickness theory are derived as follows:
From [4], [7], [10], and conservation of bed length we have

$$W_f = e_o f = ef = h \left[\frac{\sin (\gamma^* - \beta_1)}{\sin \gamma^* \sin (2\,\gamma^* - \beta_1)} \right] = h \left[\frac{\sin (2\,\gamma - \Theta_2 - \gamma^*)}{\sin \gamma^* \sin (2\,\gamma - \Theta_2)} \right] \qquad [33]$$

from [3] and Figure 16 we have

$$W_b = eb + bg = eb + (fc_o - fc) \left[\frac{\sin (\gamma_1 + \Theta_2)}{\sin \gamma_1} \right]$$

$$= h \left[\frac{\sin (\gamma_1 - \gamma^*)}{\sin \gamma_1 \sin \gamma^*} \right] + h \left[\frac{1}{\sin \Theta_2} - \frac{1}{\sin (2\,\gamma - \Theta_2)} \right] \left[\frac{\sin (\gamma_1 + \Theta_2)}{\sin \gamma_1} \right] \qquad [34]$$

Combining we obtain

$$\left[\frac{W_f}{W_b} \right] = \left[\frac{\left[\frac{\sin (2\,\gamma - \Theta_2 - \gamma^*)}{\sin \gamma^* \sin (2\,\gamma - \Theta_2)} \right]}{\left[\frac{\sin (\gamma_1 - \gamma^*)}{\sin \gamma_1 \sin \gamma^*} \right] + \left[\frac{1}{\sin \Theta_2} - \frac{1}{\sin (2\,\gamma - \Theta_2)} \right] \left[\frac{\sin (\gamma_1 + \Theta_2)}{\sin \gamma_1} \right]} \right] \qquad [35]$$

The back-limb height H_b is given by

$$H_b = W_b \sin \delta_b = W_b \sin 2\gamma_1 \quad [36]$$

and the front-limb H_f by

$$H_f = W_f \sin \delta_f = W_f \sin 2\gamma \quad [37]$$

Combining we have

$$\left[\frac{H_b}{H_f}\right] = \left[\frac{W_b}{W_f}\right]\left[\frac{\sin 2\gamma_1}{\sin 2\gamma}\right] \quad [38]$$

Graphs of the relationship between back-limb dip and limb-width and height ratios for the fixed-axis and constant-thickness theories are given in Figures 23 and 24. It should be noted that the relationship between back-limb dip and width ratio is quite different for the two theories, whereas the height ratios are nearly identical for $\Theta_1 < 30°$. Therefore width ratios are more useful in distinguishing the two theories. Good data on either ratio will provide good constraints on the cut-off angle Θ_1, whereas the back dip δ_b provides a good constraint on the fault-bend Φ.

Although there are only two independent variables in each theory (basically the fault shape Θ_1 and Θ_2), three dimensions are required to fully represent the two theories in terms of our diagnostic quantities. Each theory is represented as a surface within the three dimensions δ_f, δ_b, and W_b/W_f. The two theories coincide along the line of intersection of the two surfaces, which is labled as the *constant-thickness* line on the fixed-axis graphs (Fig. 23) and as the *fixed-axis* line on the constant-thickness graphs (Fig. 24). In Figure 22 the two theories coincide where the fixed-axis line overlaps the constant-thickness area. These lines of coincidence correspond to the $T_o/T = 1$ lines in Figure 20.

4.3 Comparison of theory with map-scale folds

We now attempt to compare data on possible fault-propagation folds with the quantitative predictions of the theories, using the diagnostic graphs given in Figures 21–24. We have assembled data in Table 1 on nineteen relatively well constrained folds, most of which are map-scale (kilometer-scale) structures. Cross-sectional solutions to three of the folds – constructed using the theory of fault-propagation folding – are presented in Figures 9, 26, 27 and 28.

There are significant difficulties in comparing map-scale structures with theory. It is important to realize that none of these structures is completely observed, which is the almost universal situation for large-scale structures; thus we must make decisions about the origins of these folds and the success of these theories based on incomplete data. In particular the fault shape is commonly poorly known. Complexities may exist in the unobserved parts of the subsurface that are unexpected and beyond the scope of the theories. Furthermore, it is very common for map-scale structures to contain significant additional complexities such as preexisting faults, folds and unconformities, which are not specifically addressed by these simple theories. For example, Oak Ridge anticline (Figs. 26 and 27) contains major folded normal faults and Puri anticline

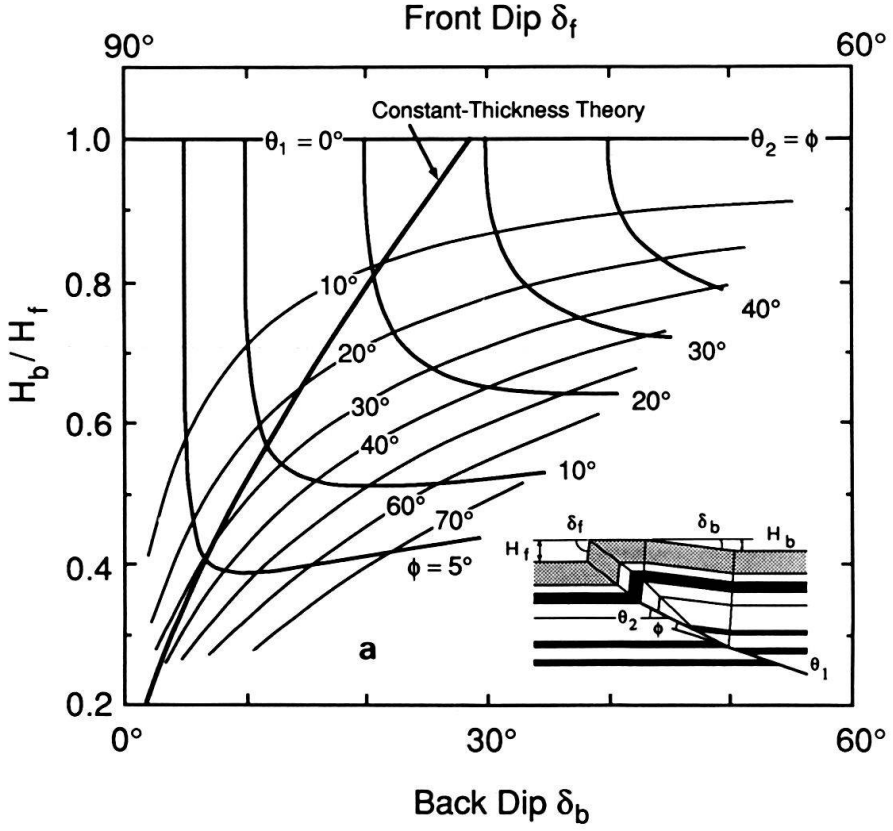
Front Dip δ_f
90°
60°
Constant-Thickness Theory
$\theta_1 = 0°$
$\theta_2 = \phi$
1.0
0.8
0.6
0.4
0.2
H_b / H_f
10°
20°
30°
40°
20°
30°
40°
10°
60°
70°
$\phi = 5°$
δ_f
δ_b
H_f
H_b
θ_2
ϕ
θ_1
a
0°
30°
60°
Back Dip δ_b

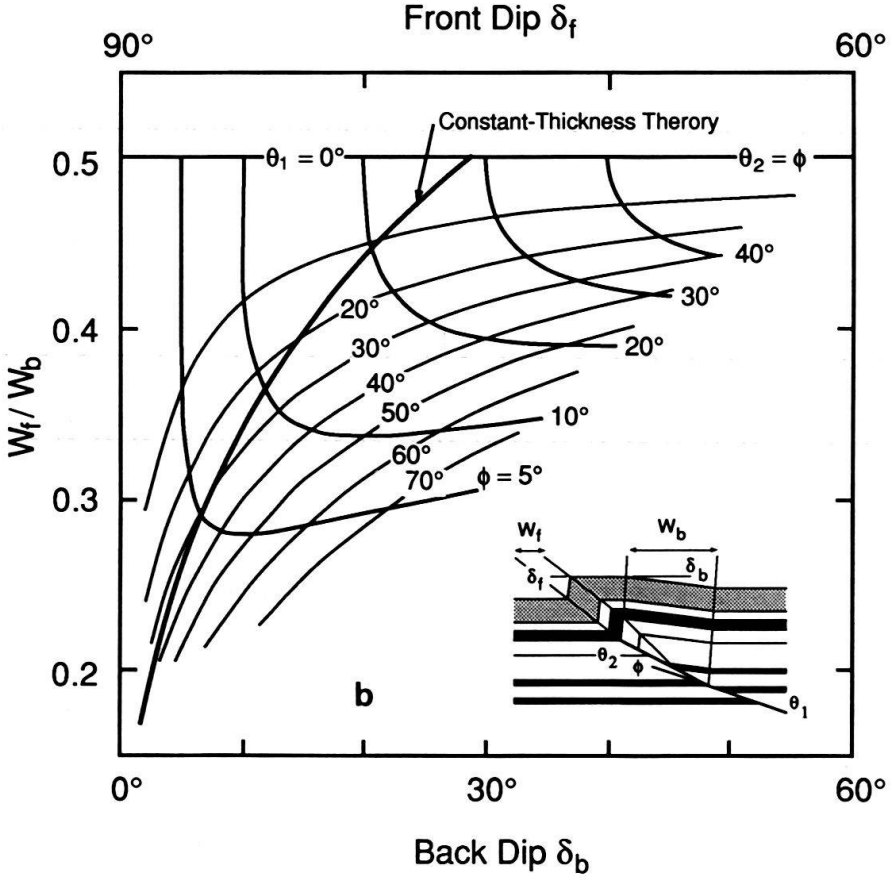
Front Dip δ_f
90°
60°
Constant-Thickness Therory
$\theta_1 = 0°$
$\theta_2 = \phi$
0.5
0.4
0.3
0.2
W_f / W_b
40°
30°
20°
30°
40°
50°
10°
60°
70°
$\phi = 5°$
W_f
W_b
δ_f
δ_b
θ_2
ϕ
θ_1
b
0°
30°
60°
Back Dip δ_b

(Fig. 28) contains a folded thrust fault. The folding of preexisting faults and angular unconformities at a map scale can usually be successfully treated with fault-bend folding theory (SUPPE 1983b) or a related theory of folding of faults (SUPPE 1986).

A further difficulty exists that is specific to the fixed-axis theory. This theory, which predicts thickening or thinning of the steep front limb assumes homogeneous deformation as a convenient simplification, which is really not to be expected in upper crustal brittle deformation. The overall thickening or thinning within the front limb would probably take place by various outcrop-scale deformation mechanisms involving faulting and folding (for example PERRY 1978; PRICE 1967). Therefore it is not clear that dips should be homogeneous. For example, Oak Ridge anticline (Figs. 26 and 27), which has very extensive drilling in the front limb, shows substantial heterogeneity in front-limb dip. Therefore, it may be difficult to accurately determine the front-limb dip in a way that is appropriate for comparison with the simple theory.

The observed front and back limb dips δ_f and δ_b of nineteen possible fault-propagation folds are summarized in Table 1 and are plotted in Figure 25 in comparison with the theoretical predictions of Figure 22. We see immediately that all the data lie within the area of the constant-thickness theory. Furthermore some data lie along the constant-thickness theory for the case of thrusts stepping up from a decollement ($\Theta_2 = \Phi$), some data lie along the line of the fixed-axis theory for back-limb dips of less than 29°, and the remainder (Yangmei and Orcutt) lie within the general field of the constant-thickness theory.

These observed limb dips (Fig. 25) show that all of the folds are possible fault-propagation folds but only some of them could be described by the fixed-axis theory. Furthermore, those folds lying along the fixed-axis theory could still be constant-thickness folds. Other observations including the ratios of limb widths and fault dips are needed to fully compare these folds with the two theories.

The ratios of limb widths (W_f/W_b) have been observed for about half of the folds in Table 1. We first consider the folds that lie well removed from the fixed-axis theory. In this case we simply wish to see if their limb widths and dips agree with the constant-thickness theory. All the folds for which width ratios are available along the decollement line ($\Theta_2 = \Phi$) are in approximate agreement with theory (Anemrakhi, Fanpaokeng and Tsaochiao). Yangmei anticline lies within the region of general constant-thickness folds and both limb dips and width ratios are well-known and in good agreement with theory. Thus these folds agree with the constant-thickness theory within the limitations of the data, suggesting that the constant-thickness theory is indeed correct. Furthermore the fact that many folds are dispersed along the constant-thickness decollement line ($\Phi = \Theta_2$) suggests that the constant-thickness theory is valid. This conclusion is further supported by the observation that all the folds in Table 1 lie within the area of the constant-thickness theory.

Fig. 23. Relationship between limb dips and ratios of (a) limb height and (b) limb width for fixed-axis fault-propagation folding, based on equations [26], [29], and [32]. The line of coincidence with the constant-thickness theory is labled. To the left of this line layer thickening occurs in the front limb, whereas to the right thinning occurs.

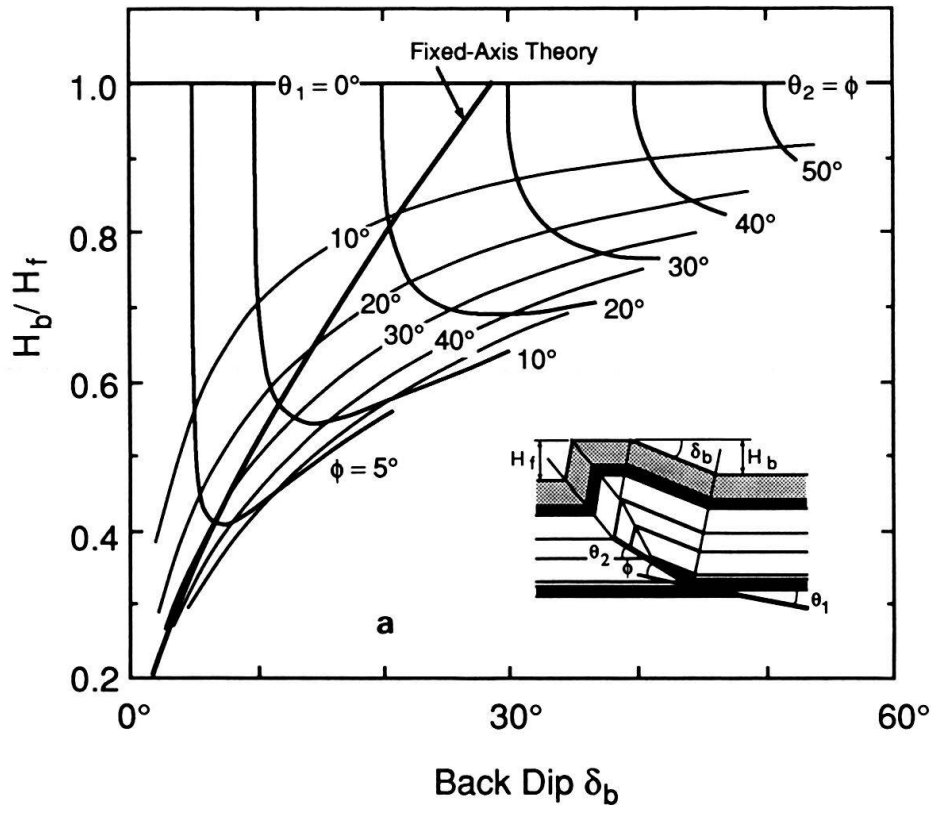
Fixed-Axis Theory
θ1 = 0°
θ2 = ϕ
50°
40°
30°
20°
10°
ϕ = 5°
Hb/ Hf
1.0
0.8
0.6
0.4
0.2
0°
30°
60°
Back Dip δb
Hf
δb
Hb
θ2
ϕ
θ1
a

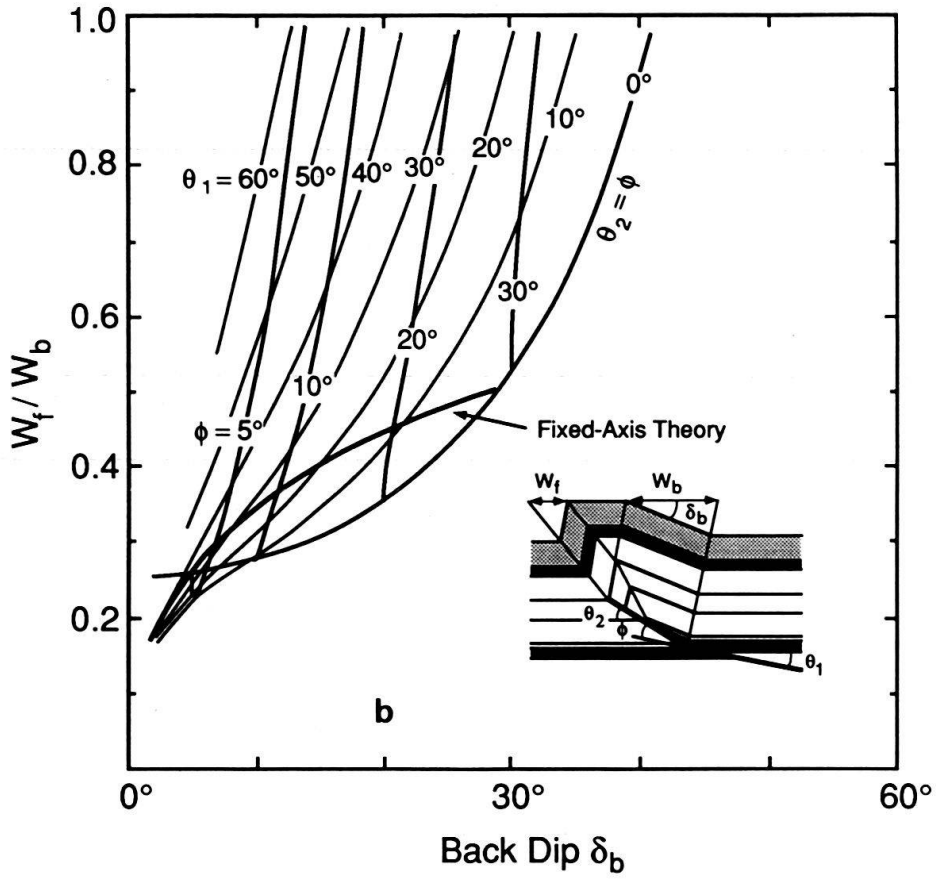
θ1 = 60°
50°
40°
30°
20°
10°
0°
θ2 = ϕ
ϕ = 5°
Fixed-Axis Theory
Wf/ Wb
1.0
0.8
0.6
0.4
0.2
0°
30°
60°
Back Dip δb
Wf
Wb
δb
θ2
ϕ
θ1
b

The folds lying along the line of the fixed-axis theory are more difficult to analyze because to distinguish the two theories we must know limb widths quite well or also have information on fault shape. Oak Ridge and Meilin both agree well with the fixed-axis theory but not uniquely given the available data, as discussed below. Abbs Valley has an added complexity to the shape of the crest such that its width ratio can be interpreted as 0.54 or 0.36, which is in agreement with either theory. Not particularly good data from Evitts Mountain also agrees with the fixed-axis theory stepping up from a decollement or with a general constant-thickness solution; however data on fault dip are not available to distinguish these possibilities. The width ratios of Willem Sophia and Belgian are not well-known but appear more consistent with the fixed-axis theory. In summary we have very limited data on width ratios of the possible fixed-axis folds; these data do not appear, on the whole, to agree well with the constant-thickness theory. A more complete analysis of Meilin anticline given below suggests that it is more probably a fixed-axis fold. Thus while some folds appear to agree with the fixed-axis theory, the scope of its geologic applicability remains an open issue until more complete data are available.

4.3.1 Oak Ridge anticline, Ventura basin, California

The best constrained cross section of a map-scale fault-propagation fold that we have is of Oak Ridge anticline in the Ventura basin, California (Figs. 26 and 27). The major weaknesses of the cross sections for our purposes are that preexisting normal faults are present within the structure – the most important being the Oak Ridge fault – and the fault that causes the fault-propagation fold has apparently not been drilled, so that its location and shape must be predicted using theory. Nevertheless it is an unusually well documented structure because of extensive deep drilling on the limbs; the South Mountain oil field lies on the gentle south limb and crest and the Saticoy oil field lies in the steep north limb. The regional and limb dips plus the positions of the axial surfaces are all well documented with well and surface data. The back dip is $16° \pm 1°$ and the front dip $80° \pm 10°$. These observations are in excellent agreement with the predictions of the fixed-axis theory for a thrust stepping from a decollement ($\Phi = \Theta_2 = \delta_f = 16°$ and $\delta_b = 82°$) and quite different from the predictions of the constant-thickness theory for a thrust stepping from a decollement ($\Phi = \Theta_2 = \delta_f = 16°$ and $\delta_b = 121°$). Nevertheless we do not know that the thrust steps from a decollement therefore we cannot exclude the constant-thickness theory ($\Theta_1 = 20°$, $\Phi = 14°$, and $\Theta_2 = 34°$). Figure 27 is a cross-section based on the constant-thickness theory. Thus the cross-section in Figure 26 agrees with the data and the fixed-axis theory but it is not unique. If we could accurately measure the ratio of limb widths in Figure 26 we could distinguish the theories, however the impingement of a fold to the south allows the

Fig. 24. Relationship between limb dips and ratios of (a) limb height and (b) limb width for constant-thickness fault-propagation folding, based on equations [35] and [38]. The line of coincidence with the fixed-axis theory is labled. To the left of the line in Figure (a) and below the line in Figure (b) beds move from the front limb to the crest; whereas to the right of the line in Figure (a) and above the line in Figure (b) beds move from the crest to the front limb.

Table 1: Data on Possible Fault-Propagation Folds

Anticline	Back Dip	Front Dip	Regional	True δ_b	True δ_f	W_f / W_b	Reference
Abbs Valley, U.S.A.	10°±2°	85°±5°	−0.5°	10.5°	84.5°	.54 or .36	ENGLAND 1968
Anemrakhi, Greece	25°±2°	105°±5°	3°±2°	22°	108°	.33–.34	unpublished data IFP
Belgian, U.S.A.	25°	75°±5°	−2°±1°	27°	73°	>.38	unpublished data
Beverly Hills, U.S.A.	29°	77°±5°	2°±2°	27°	79°	—	WRIGHT 1990 in DAVIS ET AL. 1989
Digboi, India	33°±2°	58°±5°	−3°±2°	36°–37°	55°–65°	—	MATHUR & EVANS 1964
E. Anschutz Ranch, U.S.A	98°-113°	22°–26°	−3°±1°	19°–23°	95°-110°	—	DOW 1988
Evitts Mtn, U.S.A.	18°±3°	80°±5°	—	18°	80°	≤.5	DE WITT & COLTON 1964
Fanpaokeng, Taiwan	21°±4°	78°	−13°±2°	34°	65°	≤.67	NAMSON 1984
Hope's Nose, Devon	118°	0°	−23°	23°	95°	—	WILLIAMS & CHAPMAN 1983
Meilin, Taiwan	24°±2°	77°±8°	3°±3°	21°	80°	≤.5	Figure 9
Oak Ridge, U.S.A.	21°±1°	75°±10°	5°	16°	80°	—	Figures 26 & 27
Orcutt, U.S.A.	19.5°±1°	70°±5°	2°	17.5°	72°	.34–.40	NAMSON & DAVIS 1990
Puri, P.N.G.	36°±3°	58°±1°	1°±1°	35°	59°	—	Figure 28
Tsaochiao, Taiwan	−18°±1°	131°±3°	−43°±2°	25°	88°	.36–.45	Figure 7
Umtanum Ridge, U.S.A.	17.5°±3°	85°±5°	1°	16.5°	86°	—	PRICE 1982
Willem Sophia, Ned.	12°	90°±5°	−15°±3°	27°	75°	.43	RAASVELDT in SAX 1946
Wills Mtn, U.S.A.	26°	90°	—	26°	90°	—	PERRY 1978
Yakataga, Alaska	24°±2°	90°±3°	1°±1°	23°	91°	—	Figure 8
Yangmei, Taiwan	20°±2°	66°±5°	5°±1°	15°	71°	.45±.05	unpublished data

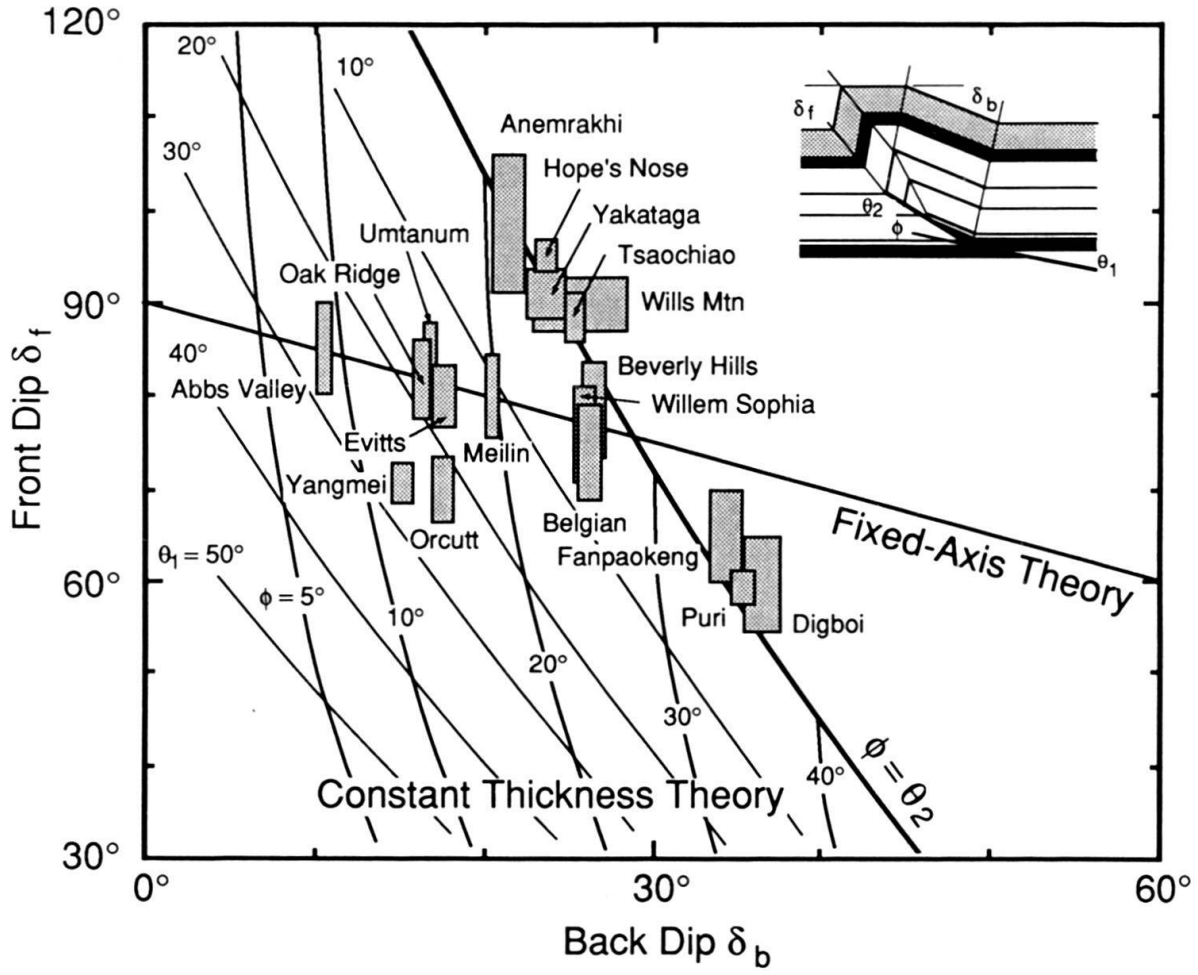

Fig. 25. Relationship between front dip and back dip (Fig. 22) for the folds listed in Table 1. The folds that lie along the line $\Phi = \Theta_2$ plus Yangmei and Orcutt are in agreement with the constant-thickness theory. All the folds that lie along the fixed-axis line lie within the area of the constant-thickness theory; therefore limb widths are required to distinguish the two theories for these folds. None of those that have limb-width observations (Abbs Valley, Belgian, Meilin and Willem Sophia), except possibly Abbs Valley, have values of W_f/W_b that agree with the constant-thickness theory.

measurement of only a minimum back-limb width. Furthermore the front-limb width is not well constrained. The fixed-axis theory predicts a ratio W_f/W_b of 0.5 whereas the constant-thickness theory predicts 0.4. In a later section we show that the Oak Ridge anticline displays the back-limb growth structure predicted from the kinematics of fault-propagation folding. Therefore the Oak Ridge anticline seems clearly to be a fault-propagation fold but it is not yet clear which theory fits it best.

The major reverse fault drilled in the steep front limb, the Oak Ridge fault, is considered a folded preexisting normal fault because if it is unfolded with the beds using the theory of folding of preexisting faults it has an original north dip of about 65–70°. This fault may have undergone some minor reactivation after folding, as shown in Figure 26. The interpretation of the Oak Ridge fault as a folded normal fault has been given by Suppe (1985, p. 497) and Namson (1987) based upon regional considerations.

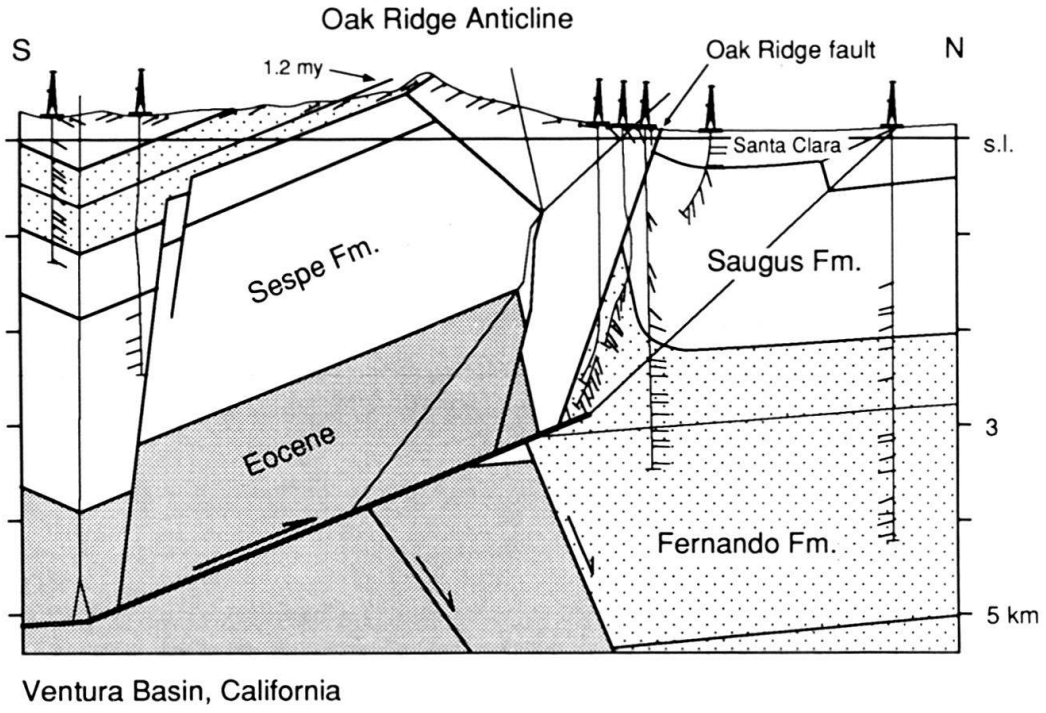

Fig. 26. Cross section of the Oak Ridge anticline Ventura Basin, California based upon the fixed-axis theory. The Oak Ridge fault is interpreted to be an old normal fault that is basically unrelated to the fault-propagation fold, although it may have reactivated to a minor extent in its present overturned position. Unfolding of the Oak Ridge fault yields an original dip of about 65° based on the technique of SUPPE (1986), which is consistent with the normal-fault interpretation. Cross section is based on subsurface data of YEATS (1988) and surface mapping of BADDLEY (1954). The subsurface geology of the south limb is based on numerous wells not shown (YEATS, personal communication 1989).

4.3.2 Meilin anticline, Taiwan

Meilin anticline at the front of the active fold-and-thrust belt of western Taiwan (Fig. 9) has a width ratio of ≤ 0.5 which agrees with the fixed-axis theory stepping up from a decollement. Nevertheless this shape also agrees with the constant-thickness theory for $\Theta_1 = 17°$ and $\Phi = 21°$. The fixed-axis theory is considered the correct one for Meilin because the beds just above the fault in the well are Talu Shale, a known decollement horizon, whereas the constant-thickness solution makes less sense in the regional context (SUPPE 1986).

4.3.3 Puri anticline, Papua New Guinea

The Puri anticline (Fig. 28) in the fold-and-thrust belt of Papua New Guinea is relatively well constrained by surface data, one well with several deviations, and unpublished seismic data, which constrains the regional dip. Its limb dips $\delta_f = 59°$ and $\delta_b = 35°$ are in good agreement with the constant-thickness theory for a thrust stepping up from a decollement $\Phi = \Theta_2$. Furthermore its shape is difficult to satisfy by other folding mechanisms, such as fault-bend folding. Therefore it is interpreted in Figure 28 as a constant-thickness fault-propagation fold, although this interpretation is by no

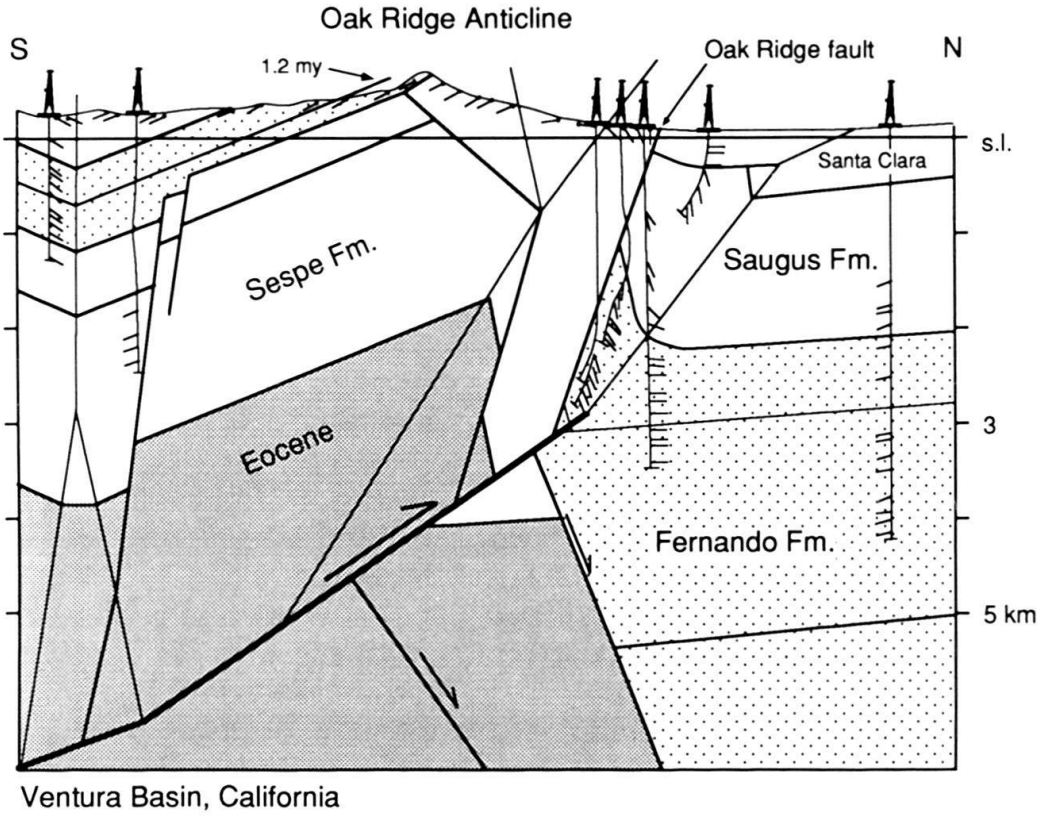

Fig. 27. Cross section of the Oak Ridge anticline Ventura Basin, California based upon the constant-thickness theory (compare fixed-axis solution Fig. 26).

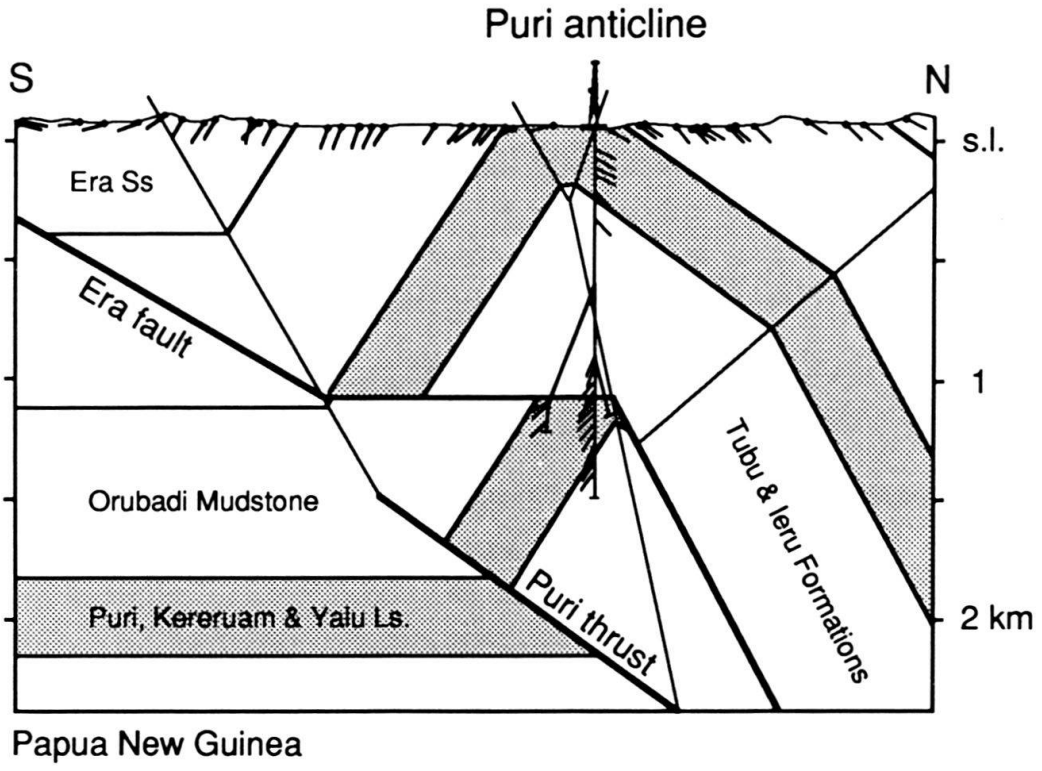

Fig. 28. Puri anticline, Papua New Guinea.

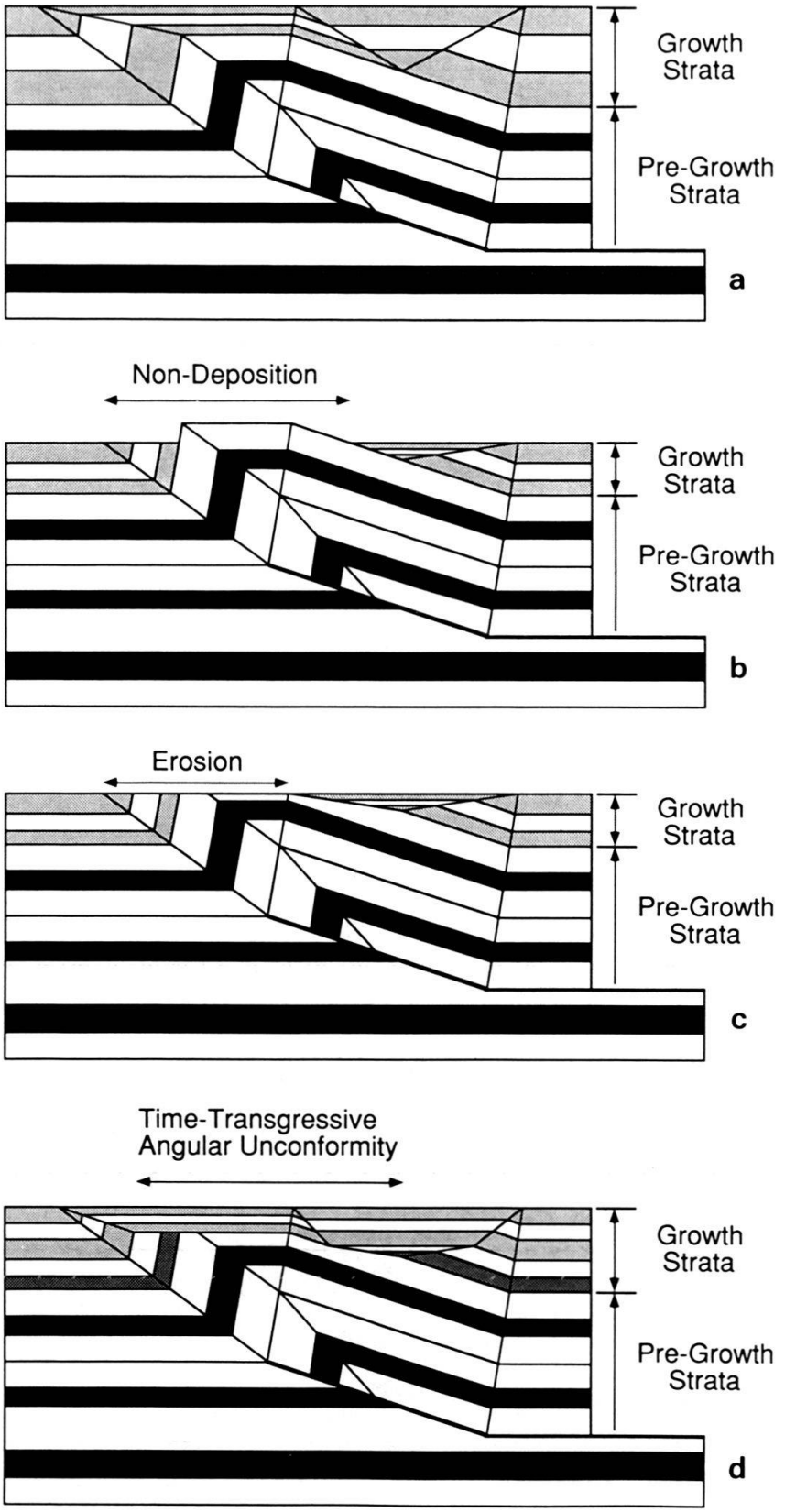

Fig. 29. Models of fixed-axis growth fault-propagation folds at various sedimentation rates. The models are constructed with sedimentation rate constant relative to fault-slip rate, except for Figure (d) which first deforms with an eroding crest and later with deposition over the crest.

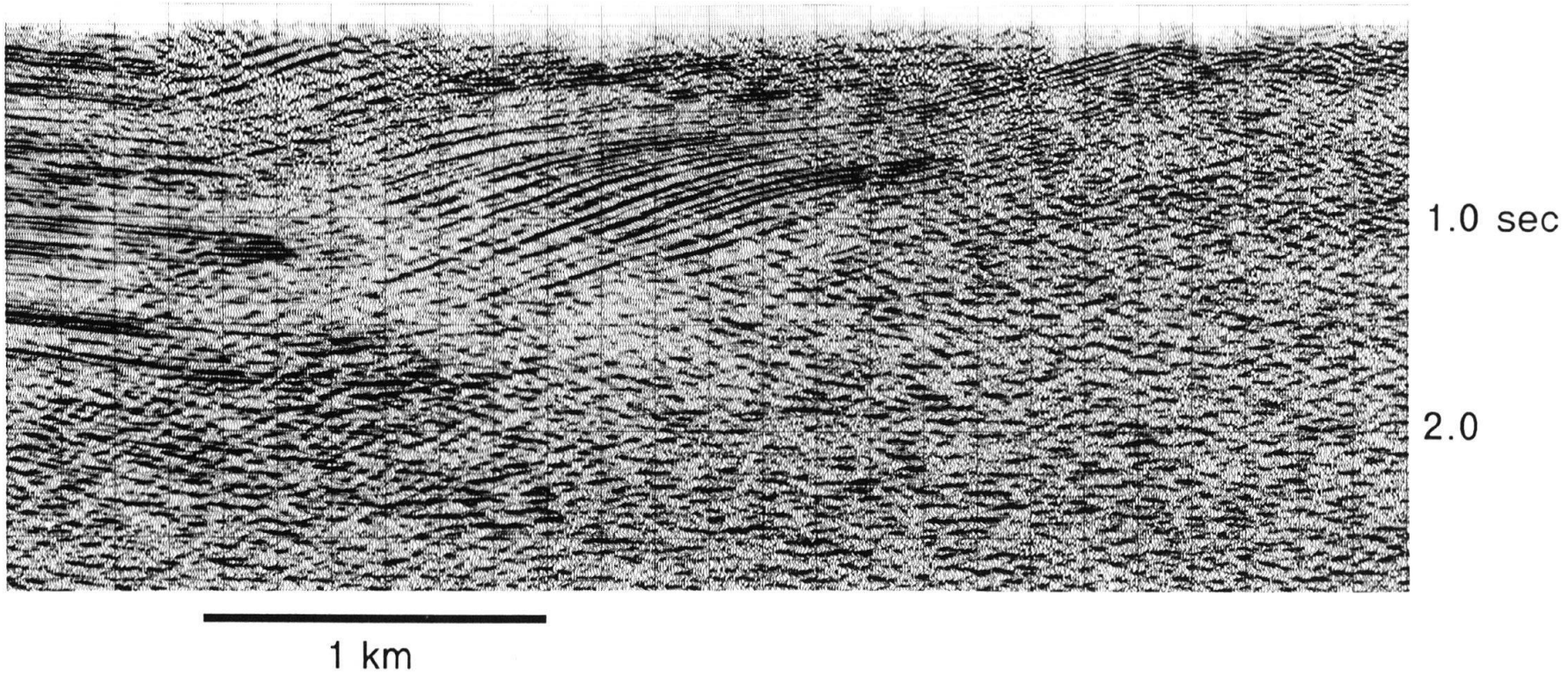

Fig. 30. Seismic section of the back limb of the Oak Ridge anticline down plunge from Figures 26 and 27. This seismic line shows a triangular region of flat dips above the long back limb which is similar to that predicted for fault-propagation folding (Fig. 29).

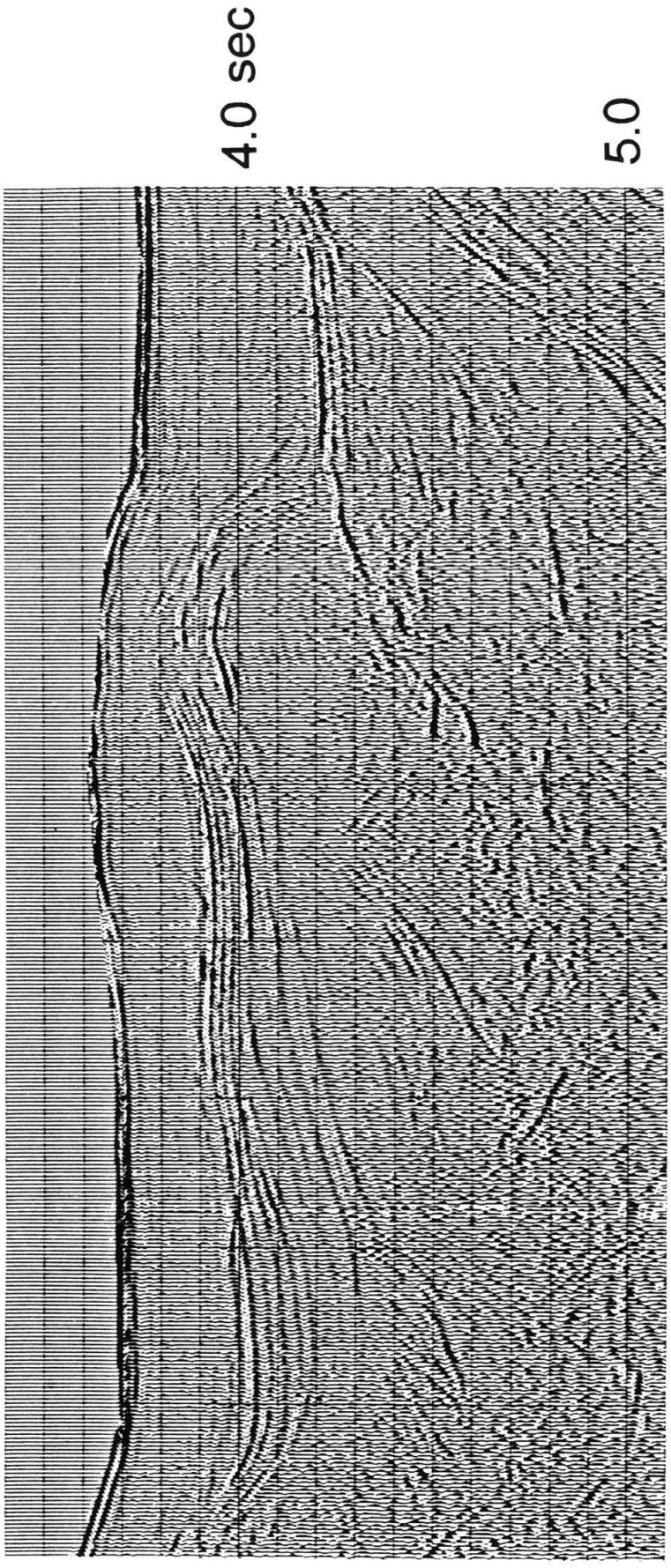

Fig. 31. Seismic section from the deep-water Perdido foldbelt of the Gulf of Mexico (Mount & Suppe 1990) showing the back-limb growth predicted for fault-propagation folds. Seismic profile provided by Texaco USA.

means certain. Note that the flat fault encountered in the wells cannot be the fault that produces the fold because the same dips are present above and below; this fault is interpreted to be a preexisting thrust because when it is extrapolated southward from the wells through the front syncline using fault-bend folding theory it projects to the surface trace of the Era fault.

5. Growth fault-propagation folding

The kinematic properties of fault-propagation folding make specific predictions about the shapes of folds within *growth strata,* that is within the beds that were deposited during deformation. These growth strata provide a powerful test of the kinematic predictions of the theory of fault-propagation folding. The theory of growth folding is beyond the scope of this paper and is presented elsewhere (Suppe et al. 1990). Simply stated the limbs of the fold grow by kink-band migration with constant limb-dip. Therefore the kink band should narrow upward in a predictable way through the growth stratigraphic section.

A set of models of a fixed-axis fault-propagation fold are given in Figure 29. Here we only consider the back limbs because they are easily imaged seismically whereas front limbs are not normally imaged. The shapes predicted for the back limbs are the same for the constant-thickness theory. The key property of back limbs of fault-propagation folds is that both axial surfaces move outward with respect to the rock. The triangle of flat dipping beds over the back limb within the growth section records the progressive widening of the back limb through time. The bottom of the triangle records the initial position of the two axial surfaces in the rock before deformation.

The predictions of the models are observed on seismic profiles of growth fault-propagation folds. Figure 30 is a seismic profile of the back limb of the Oak Ridge anticline down plunge from Figure 26. It displays the characteristic triangular region of flat dips within the growth strata. This observation provides further confirmation that the Oak Ridge anticline is a fault-propagation fold. Figure 31 is a seismic profile of a growth fault-propagation fold from the Perdido foldbelt, Gulf of Mexico, which also displays the characteristic triangle of flat dips over the back limb. Other examples of growth fault-propagation folds are given by Suppe et al. (1990).

6. Conclusions and summary

Some thrust faults are observed in outcrop to terminate in asymmetric folds. Quantitative and qualitative analysis of their shapes shows that they are in agreement with the concept of fault-propagation folding in which the folds grow progressively and self-similarly at the fault tip during thrust-fault propagation. Furthermore the shapes of folds within growth strata on the back limbs of fault-propagation folds are in agreement with this kinematic model. In addition many tight asymmetric synclines below thrust faults and tight anticlines above thrust faults can be interpreted as fragments of fault-propagation folds that have broken through and been dismembered.

Two quantitative theories of fault-propagation folding have been presented which subsume many of the main phenomena that might be expected in natural folds under brittle conditions, including conservation of layer thickness, thickening or thinning of

the front limb, and bedding-parallel shear within the thrust sheet. These theories have been cast in terms of easily measured diagnostic parameters including front and back limbs dips and ratios of limb widths, which allow prediction of subsurface fault and fold geometry. A number of outcrop and map-scale folds are shown to have shapes that are in good quantitative agreement with the constant-thickness theory, whereas other less well constrained folds appear to agree with the fixed-axis theory.

The general qualitative and quantitative agreement between the predicted and observed shapes of folds in both preexisting and growth strata provides strong support for the hypothesis of fault-propagation folding.

Acknowledgments

Many individuals and organizations have contributed to the development and testing of the theory of fault-propagation folding. Professor H.P. Laubscher, in whose honor this paper is written, inspired Suppe by both conversations and written papers (for example Laubscher 1961, 1965) to attempt quantitative geometric and kinematic analysis of large-scale structures. Robert Hatcher led a field trip in 1982 to an outcrop in the southern Appalachians that sparked for Suppe the idea of fault-propagation folding and the constant-thickness theory. The theory was first tested extensively on map-scale structures (Suppe 1983a) with the help of the Chinese Petroleum Corporation during 1982–83 while Suppe was a visiting professor at the National Taiwan University, supported by the National Science Council ROC. Jim Helwig and Wes Wallis of ARCO kindly led Suppe to the outcrops of fault-propagation folds in Alaska (Figs. 1 and 8). G.T.C. Chou and S.C. Hook of Texaco were visiting professors at Princeton University in Fall 1985 during which many seismic lines were studied, which confirmed the kinematic predictions of fault-propagation folding (Figs. 30–31). Also, Chou first recognized the kinematic questions raised by the constant-thickness theory at low step-up angles, which led us to develop the fixed-axis theory in Spring 1986. Robert Yeats provided helpful insight into Oak Ridge anticline (Figs. 26 and 27). Data on Puri anticline were provided by the Geological Survey of Papua New Guinea. We thank Steve Boyer, Peter Geiser, Wayne Narr, and Thomas Noack for reviews of the manuscript. Financial support for this research was provided in part by Texaco, ARCO and USGS NEHRA grant 14-08-0001-G1699.

REFERENCES

Ave'Lallemant, H.G., Kelly, J.S. & Phelps, J.C. 1987: Kinematic analysis of range-front thrust faulting near Anaktuvuk Pass, north-central Brooks Range, Alaska. In: Alaskan North Slope Geology. Pacific Section Soc. Econ. Paleont. Mineral. and Alaska Geol. Soc., 639–645.

Baddley, E.R. 1954: Geology of the South Mountain oil field, Ventura County. California Div. of Mines Bull. 170, map sheet 29.

Benvenuto, G.L. & Price, R.A. 1979: Structural evolution of the Hosmer thrust sheet southeastern British Columbia. Canad. Petroleum Geol. Bull. 27, 360–394.

Berg, R.R. 1962: Mountain flank thrusting in Rocky Mountain foreland, Wyoming and Colorado. Amer. Assoc. Petroleum Geol. Bull. 46, 2019–2032.

Berger, P. & Johnson, A. 1980: First-order analysis of deformation of a thrust sheet over a ramp. Tectonophysics 70, T9-T24.

Brown, S.P. & Spang, J.H. 1978: Geometry and mechanical relationship of folds to thrust fault propagation using a minor thrust in the Front Ranges of the Canadian Rocky Mountains. Canad. Petroleum Geol. Bull. 26, 551–571.

Dahlstrom, C.D.A. 1970: Structural geology in the eastern margin of the Canadian Rocky Mountains. Canad. Petroleum Geol. Bull. 18, 332–406.

Danilchik, W., Rothrock, H.E. & Wagner, H.C. 1955: Geology of anthracite in the western part of the Shenandoah quadrangle, Pennsylvania. U.S. Geol. Surv., Coal Investigation Map C-21.

Davis, T.L., Namson, J.S. & Yerkes, R.F. 1989: Structural analysis of seismically active compression in the Los Angeles basin and implications for seismic risk. J. Geophys. Res. 94, 9644–9664.

de Witt, W. & Colton, G.W. 1964: Bedrock geology of the Evitts Creek and Pattersons Creek quadrangles, Maryland, Pennsylvania, and West Virginia. United States Geol. Surv. Bull. 1173.

Douglas, R.J.W. 1950: Callum Creek, Langford Creek, and Gap map-areas, Alberta. Geol. Surv. Canada Mem. 255.

Dow, R.L. 1988: Manipulation of the integrated data base: a case study of the East Anschutz Ranch. Mountain Geologist 25, 39–46.

Elliot, D. 1976: The energy balance and deformation mechanisms of thrust sheets. Phil. Trans. R. Soc., Lond. A 283, 289–312.

England, K.J. 1968: Geologic map of the Bramwell quadrangle, West Virginia-Virginia. United States Geol. Surv. Geologic Quadrangle Map GQ-745.

Fox, F.G. 1959: Structure and accumulation of hydrocarbons in southern Foothills, Alberta, Canada. Amer. Assoc. Petroleum Geol. Bull. 43, 992–1025.

Gries, R. 1983: Oil and gas prospecting beneath Precambrian of foreland thrust plates in Rocky Mountains. Amer. Assoc. Petroleum Geol. Bull. 67, 1–28.

Harris, L.D. 1970: Details of thin-skinned tectonics in parts of Valley and Ridge and Cumberland Plateau provinces of southern Appalachians. In: Studies in Appalachian Geology, Central and Southern (Ed. by Fisher, G.W. et al.). Wiley-Interscience, New York, 161–173.

Heim, A. 1919: Geologie der Schweiz. Tauchnitz, Leipzig.

Lamerson, P.R. 1982: The fossil basin area and its relationship to the Absaroka thrust fault system. In: Geologic Studies of the Cordilleran Thrust Belt (Ed. by Powers, R.B.). Rocky Mountain Assoc. Geologists, 279–340.

Laubscher, H.P. 1961: Die Fernschubhypothese der Jurafaltung. Eclogae geol. Helv. 54, 221–282.

— 1965: Ein kinematisches Modell der Jurafaltung. Eclogae geol. Helv. 58, 231–318.

Mathur, L.P. & Evans, P. 1964: Oil in India. 22nd International Geol. Congress, New Delhi.

Matthews, Vincent, III, (editor) 1978: Laramide folding associated with basement block faulting in the western United States. Geol. Soc. Amer. Mem. 151.

Mosar, J. & Suppe, J. 1990: Role of shear in fault-propagation folding. In: Thrust Tectonics (Ed. by McClay, K.). Unwin Hyman, London (in press).

Mount, V. & Suppe, J. 1990: Seismic structural analysis of the deep-water Perdido fold belt, Alaminos Canyon, northwest Gulf of Mexico. In: Future Petroleum Provinces of North America. Amer. Assoc. Petroleum Geol. Mem. (in press).

Namson, J. 1984: Detailed structural analysis of the western foothills belt in the Miaoli-Hsinchu area, Taiwan: III. northern part. Petroleum Geol. Taiwan. 20, 35–52.

— 1987: Structural transect through the Ventura basin and western Transverse Ranges. In: Structural evolution of the western Transverse Ranges (Ed. by Davis, T.L. & Namson, J.). Pacific Section Soc. of Economic Paleont. Mineral. 48A, 29–41.

Namson, J. & Davis, T.L. 1990: Late Cenozoic fold-and-thrust belt of the southern Coast Ranges and Santa Maria basin, California. Amer. Assoc. Petroleum Geol. Bull. 74, 467–492.

Narr, W. 1990: Deformational behavior and kinematics of basement-involved structures and joint spacing in sedimentary rocks. Ph. D. Dissertation, Princeton University.

Narr, W. & Suppe, J. 1989: Kinematics of low-temperature, basement-involved compressive structures. Geol. Soc. Amer. Abstr. Prog. 21, 137.

Perry, W.J., Jr. 1978: Sequential deformation in the central Appalachians. Amer. J. of Sci. 278, 518–542.

Price, E.H. 1982: Structural geometry, strain distribution, and mechanical evolution of eastern Umtanum Ridge, and a comparison with other selected localities within Yakima fold structures, south-central Washington. Ph. D. Dissertation, Washington State Univ.

Price, R.A. 1967: The tectonic significance of mesoscopic subfabrics in the southern Rocky Mountains of Alberta and British Columbia. Canadian J. Earth Sci. 4, 39–70.

Prucha, J.J., Graham, J.A. & Nickelson, R.P. 1965: Basement controlled deformation in Wyoming province of Rocky Mountain foreland. Amer. Assoc. Petroleum Geol. Bull. 49, 966–992.

Rich, J.L. 1932: Mechanics of low-angle overthrust faulting as illustrated by Cumberland thrust block, Virginia, Kentucky, and Tennessee. Amer. Assoc. Petroleum Geol. Bull. 18, 1584–1596.

Sax, H.G. 1946: De tektoniek van het Carboon in het Zuid Limburgsch Mijngebied. Geol. Stichting. Med. ser. CI-1, n. 3.

Stearns, D.W. 1971: Mechanisms of drape folding in the Wyoming province. In: 23rd Field Conference Guidebook, Wyoming Tectonics Symposium. Wyoming Geol. Assoc., 125–143.

— 1978: Faulting and forced folding in the Rocky Mountains foreland. In: Laramide folding associated with basement block faulting in the western United States (Ed. by MATTHEWS, V.). Geol. Soc. Amer. Mem. 151, 1–37.

STOCKMAL, G.S. 1979: Structural Geology of the Northern Termination of the Lewis Thrust, Front Ranges, Southern Canadian Rocky Mountains. M.S. Thesis, Univ. Calgary, Canada.

SUPPE, J. 1980: A retrodeformable cross-section of northern Taiwan. Proc. Geol. Soc. China. 23, 46–55.

— 1983a: Some Theory of Parallel Folding Useful in Predicting Subsurface Structure. Department of Geol. and Geophys. Sci., Princeton Univ., and Taiwan Petroleum Explor. Div., Chinese Petroleum Corporation, 1–11.

— 1983b: Geometry and kinematics of fault-bend folding. Amer. J. Sci. 283, 684–721.

— 1984: Seismic interpretation of compressively reactivated normal fault near Hsinchu, western Taiwan. Petroleum Geol. Taiwan. 20, 85–96.

— 1985: Principles of Structural Geology. Prentice-Hall Inc., Englewood Cliffs, New Jersey.

— 1986: Reactivated normal faults in the western Taiwan fold-and-thrust belt. Mem. Geol. Soc. China 7, 187–200.

SUPPE, J., CHOU, G.T. & HOOK, S.C. 1990: Determination of rates of fold growth and fault slip from growth strata. In: Thrust Tectonics (Ed. by MCCLAY, K.). Unwin Hyman, London (in press).

SUPPE, J. & MEDWEDEFF, D.A. 1984: Fault-propagation folding. Geol. Soc. Amer. Abst. Prog. 16, 670.

WILLIAMS, G. & CHAPMAN, T. 1983: Strain development in the hangingwalls of thrusts due to their slip/propagation rate. A dislocation model. J. Struct. Geol. 5, 563–571.

WILLIS, B. & WILLIS, R. 1934: Geologic Structures. McGraw-Hill, New York.

WILTSCHKO, D.V. & EASTMAN, D. 1983: Role of basement warps and faults in localizing thrust fault ramps. Geol. Soc. Amer. Mem. 158, 177–190.

WOODWARD, N.B., BOYER, S.E. & SUPPE, J. 1985: An outline of balanced cross sections, 2nd ed. University Tennessee, Dept. Geological Sci., Studies Geol. 11.

YEATS, R.S. 1988: Late Quaternary slip rate on the Oak Ridge fault, Transverse Ranges, California: implications for seismic risk. Jour. Geophys. Res. 93, 12137–12149.

Manuscript received 17 April 1990
Revised version accepted 9 August 1990